Trap-and-trigger determination of absolute radical quantum yields in radical-based treatment processes

Yiqi Yan[1, 2], Yunxiang Meng[1, 2], Kanying Miu[1, 2], Jannis Wenk[3], Cort Anastasio[4], Richard Spinney[5], Chong-Jian Tang[1, 2,*] and Ruiyang Xiao [1, 2,*]

[1] Institute of Environmental Engineering, School of Metallurgy and Environment, Central South University, Changsha, 410083, China

[2] Chinese National Engineering Research Center for Control & Treatment of Heavy Metal Pollution, Changsha, 410083, China

[3] Department of Chemical Engineering, Water Innovation & Research Centre (WIRC@Bath), University of Bath, BA2 7AY, UK

[4] Department of Land, Air, and Water Resource, University of California, Davis, California 95616, United States

[5] Department of Chemistry and Biochemistry, the Ohio State University, Columbus, Ohio, 43210, U.S.

*To whom correspondence should be addressed. C.J. Tang, Phone: +86–731–88830511, Email: chjtang@csu.edu.cn; R.X. Phone: +86–731–88830875, Email: xiao.53@csu.edu.cn.

ABSTRACT

The absolute radical quantum yield (Φ) is a critical parameter to evaluate the efficiency of radical-based processes in engineered water treatment. However, measuring Φ is fraught with challenges, as current quantification methods lack selectivity, specificity and anti-interference capabilities, resulting in significant error propagation. Herein, a direct and reliable time-resolved technique to determine Φ for commonly used radical precursors in advanced oxidation processes is reported. For H_2O_2 and peroxydisulfate (PDS), the values of $\Phi_{\bullet OH}$ and $\Phi_{SO_4^{\bullet-}}$ at 266 nm were measured to be 1.10 ± 0.01 and 1.46 ± 0.05, respectively. For peroxymonosulfate (PMS), we developed a new approach to determine $\Phi_{\bullet OH}^{PMS}$ with terephthalic acid as a trap-and-trigger probe in the non-steady state system. For the first time, the $\Phi_{\bullet OH}^{PMS}$ value was measured to be 0.56 by the direct method, which is stoichiometrically equal to $\Phi_{SO_4^{\bullet-}}^{PMS}$ (0.57 ± 0.02). Additionally, radical formation mechanisms were elucidated by density function theory (DFT) calculations. The theoretical results showed that the highest occupied molecular orbital of the radical precursors are O-O antibonding orbitals, facilitating the destabilization of the peroxy bond for radical formation. Electronic structures of these precursors were compared, aiming to rationalize the tendency of the Φ values we observed. Overall, this time-resolved technique with specific probes can be used as a reliable tool to determine Φ, serving as a scientific basis for accurate performance evaluation of diverse radical-based treatment processes.

Keywords: radical quantum yield; radical-based treatment; reaction mechanisms; time-resolved technique.

Synopsis: This study presents a direct and reliable method for determining absolute

radical quantum yields, offering a valuable means to accurately evaluate the efficiency of radical-based treatment processes.

1. INTRODUCTION

Rapid industrial and urbanized development have brought various deleterious micropollutants into aquatic systems, posing non-negligible threats to human and ecosystem health.[1, 2] Conventional water treatment technologies such as filtration, adsorption and biodegradation exhibit low removal efficiency for many of these micropollutants.[3, 4] To this end, advanced oxidation processes (AOPs) emerged as a group of cutting-edge decontamination technology.[5, 6] AOPs generate strong oxidative radicals, such as hydroxyl ($^{\bullet}OH$), sulfate ($SO_4^{\bullet-}$) and chlorine radicals ($Cl^{\bullet}/Cl_2^{\bullet-}$), ultimately degrading or even mineralizing recalcitrant micropollutants.[7-9]

In the evaluation of performance for different UV-based AOPs, the radical quantum yield (Φ, unitless) is a critical parameter.[10] It measures the efficiency of a photochemical reaction in generating radicals, and is defined as the ratio of the number of radicals formed to the number of photons absorbed:[11]

$$\Phi = \frac{\text{the number of radicals formed through photolysis}}{\text{the number of photons absorbed}} \quad (1)$$

However, determining Φ for radicals can be difficult due to the scarcity of reliable methods for calibrating these transient radical species. Although chemical probes have been intensively used to indirectly quantify resulting radicals for the determination of Φ,[12, 13] cautions must be exerted for an appropriate selection of probe compounds: (*i*) Many probes can react with multiple radicals to form same products,[14, 15] complicating quantification of different radicals, ultimately resulting in misestimation of Φ values. For example, benzoic acid is widely adopted as a probe compound for radical identification and quantification of $^{\bullet}OH$ and $SO_4^{\bullet-}$ in a system.[16, 17]

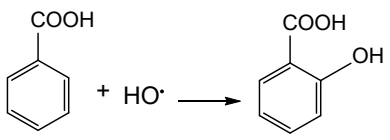

(2)

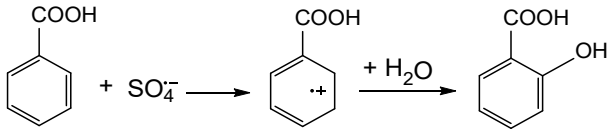

(3)

Nevertheless, the product that can be detected (*i.e.,* salicylic acid) with these two radicals is the same. (*ii*) Many probes do not always exhibit an exclusive selectivity.[18, 19] The reaction rate constant (k) of $^{\bullet}OH$ with the probe methanol is 9.7×10^8 M^{-1} s^{-1}, while its k value with H_2O_2 is 2.7×10^7 M^{-1} s^{-1}.[20] The comparable k values indicate a competition of H_2O_2 with methanol for $^{\bullet}OH$ at similar concentrations, resulting in error propagation for Φ. (*iii*) Side-reaction interference of probe and target radicals perturb the Φ determination.[21, 22] Yu *et al.* used Cl^- as a probe to measure the $\Phi_{\bullet OH}$ produced in the photolysis of H_2O_2.[23] In their system, 16 possible reaction pathways were considered which presented an obstacle for extrapolation back to initial $^{\bullet}OH$ concentration. Therefore, it is necessary to seek more direct and reliable alternatives to determine Φ for radical formation.

Advancements of time-resolved laser flash photolysis (LFP) have opened up new horizons for transient species kinetic investigations, including improved features, such as better temporal resolution (~10^{-9} s), rapid response speeds, and lower detection limits (absorbance less than 5×10^{-5}).[24-26] For environmentally relevant studies, LFP was widely exploited to investigate the transformation of micropollutants triggered by radicals and other reactive species (*e.g.*, excited triplet states of compounds).[27, 28] In particular, Canonica and von Gunten made many pioneering and significant contributions to characterize the photochemical transformation of micropollutants in sunlit natural waters.[29-31] The gradual recognition of its implementation inspires potential utilization for real-time visualization of transient species and direct determination of their Φ values in radical-based treatment processes. Note although pulse radiolysis has been also widely used to study fast reactions, the determination of

Φ values cannot be achieved with this technique, as no photons are involved in radical formation.[32, 33]

Herein, we report a direct and accurate method to determine the absolute Φ values for radicals by the LFP technique. Three typical radical precursors - H_2O_2, PDS, and peroxymonosulfate (PMS) - were selected and tested, as these precursors have been widely used to produce $^{\bullet}OH$ and $SO_4^{\bullet-}$ in AOPs for water engineering practices.[34, 35] In particular, we present a new approach to quantify the Φ value of $^{\bullet}OH$ produced from PMS using terephthalic acid (TPA) as a trap-and-trigger probe in a non-steady state system. The $\Phi_{^{\bullet}OH}^{PMS}$ value was measured by the direct method for the first time. The radical formation mechanisms were elucidated by means of density functional theory (DFT) calculations. We compared electronic structures of these precursors at the molecular level, aiming to rationalize our experimental observations. This study offers a reliable and direct Φ measurement approach for different radical species, avoiding derivatization and side-reaction interference. Our method can be used to accurately evaluate the effectiveness of radical-based treatment processes, thereby instigating informed decision-making in appropriate selection of AOPs in different treatment scenarios.

2. MATERIALS AND METHODS

2.1 Materials

Chemicals and reagents used in this study are provided in Supporting Information Text S1. The calibration of H_2O_2 concentration are described in Text S2.

2.2 Experimental approaches

For direct quantification of different radical species, an in-house built LFP

platform was used. The LFP consists of a laser, detecting unit (xenon detector lamp, monochromator, photomultiplier tube, and oscilloscope), and sampling chamber (Figure S1). The laser is used to provide a high-energy pulse for radical formation. In this study, the fourth harmonic (266 nm) oscillation of a Nd:YAG Q-switched laser was used for the excitation of working solutions. The laser pulse energy was measured by a laser energy meter (7Z01560, Vega Ophir), and the pulse width was 15 ± 1 ns. The excitation energy was set low at 21±1 mJ pulse^{-1} to avoid biphotonic events. The repetition rate was held at 10 Hz by a digital pulse generator to ensure sample full recovery between laser flashes. The flow rate of working solutions through the quartz cell (dimension of 10 × 10 × 40 mm) was controlled at 12 mL min^{-1} by a peristaltic pump (BT100-1L, LongerPump). The detecting unit allows monitoring transient species formation and decay kinetics. The detection light emitted from a pulsed xenon lamp (*ca.* 300 W) and passed through a monochromator (Omni-λ180D, ZOLIX). Then, the Oriel photomultiplier tube (PMT) converts and amplifies incident photons into an electrical signal, and real-time signal was digitized by a TDS-640A Tektronix oscilloscope (Text S3). For each trace, 512 laser shots were averaged. All experiments were conducted in triplicate under the same conditions to ensure reproducibility.

The radical quantum yield (Φ_R) from photodissociation of the precursor was calculated as:

$$\Phi_R = \frac{N(R)_0}{N(h\nu)} = \frac{C(R)_0 \times V \times N_A}{N(h\nu)} \quad (4)$$

where $N(R)_0$ and $N(h\nu)$ refer to the initial number of radicals formed (in our case $^{\bullet}OH$ and $SO_4^{\bullet-}$) and photons absorbed by the precursor, respectively; $C(R)_0$ is the initial molar concentration of radicals; and N_A represents Avogadro's number. For $SO_4^{\bullet-}$, the initial number $N(SO_4^{\bullet-})_0$ can be directly measured, as it exhibits noticeable absorbance at 450 nm.[36] For $^{\bullet}OH$, the initial number $N(^{\bullet}OH)_0$ cannot be directly obtained by

spectroscopic methods, as it does not have a characteristic absorption feature in UV and visible regions.[37] Thus, SCN^- was used as a probe, as it reacts rapidly with $^{\bullet}OH$ (eqn. 5, k =1.4 × 10^{10} M^{-1} s^{-1}),[20] forming $(SCN)_2^{\bullet-}$ with a diagnostic absorption at 475 nm:

$$^{\bullet}OH + SCN^- \rightarrow SCNOH^{\bullet-} \quad (5)$$

$$SCNOH^{\bullet-} \rightarrow SCN^{\bullet} + OH^- \quad (6)$$

$$SCN^{\bullet} + SCN^- \leftrightarrow (SCN)_2^{\bullet-} \quad (7)$$

Note, $(SCN)_2^{\bullet-}$ is in equilibrium with $SCN^{\bullet}$ (eqn. 7, K = 2 ×10^5 M^{-1}).[38] The concentration of $(SCN)_2^{\bullet-}$ remains unchanged on the microsecond time scale, making an absolute dosimetry measurement feasible. Based on the stoichiometric relation, $N(^{\bullet}OH)_0$ is equal to the initial number of $(SCN)_2^{\bullet-}$, which can be extrapolated back from the absorption profile of $(SCN)_2^{\bullet-}$.

In steady-state systems, TPA has frequently been used as a probe for $^{\bullet}OH$ quantification, as it selectively reacts with $^{\bullet}OH$ *via* hydroxylation reaction at the k of 4.4 ×10^9 M^{-1} s^{-1}.[39, 40]

$$TPA + {}^{\bullet}OH \rightarrow hTPA \quad (8)$$

The resulting hydroxyterephthalate product, hTPA, is fluorescent, resulting in high sensitivity and low background interferences.[41] For example, TPA was used to monitor $^{\bullet}OH$ production by the photolysis of nitrite and Suwannee River Fulvic Acid (SRFA).[42] Based on the fluorescence intensity of formed hTPA, the steady-concentration of $^{\bullet}OH$ from nitrite and SRFA were measured to be 4.1 fM (f for femto) and 0.6 fM, respectively. However, this quantification approach has not yet been explored in a non-steady state system. We anticipated that with LFP, negative absorption (emission) bands due to hTPA could be observed and thus the initial concentration of hTPA could be derived from a calibration. To confirm our anticipation, the steady-state fluorescence of hTPA was also measured using a fluorescence spectrophotometer (F-4600, Hitachi, Japan).

The emission wavelength was monitored from 350 to 550 nm with a step increase of 5 nm, and the excitation wavelength was set to be 315 nm.

2.3 Computational approaches

Computational studies were used to elucidate radical formation mechanism. The electronic structures of the three radical precursors (H_2O_2, PDS and PMS) were optimized using Gaussian 16 (Revision A.03).[43] The geometry optimizations of these precursors were performed at B3LYP-D3/6-31G(d,p) level of theory, and the single-point energies were calculated at a higher level of basis set (6–311G(2d,2p)) with the same functional.[44, 45] The B3LYP functional has been extensively used in geometry optimalizations, as it yields reliable electronic structures and thermodynamic results.[46, 47] Note, B3LYP-D3 refers to B3LYP functional with Grimme's GD3-BJ empirical dispersion correction[48], which can be used to exclude the interference of weak interactions. In addition, we also calculated the bond dissociation enthalpy (BDE) of several well-studied compounds (eqn. 9),[49] validating the robustness of the B3LYP-D3 functional (Table S1).

$$\mathrm{BDE} = (H^*_{\mathrm{radical[fragment1]}} - H^*_{\mathrm{radical[fragment2]}}) - H^*_{\mathrm{parent\ compound}} \quad (9)$$

where H^* represents the enthalpy of formation (kcal mol^{-1}). The accuracy of the 6–311G(2d,2p) basis set was also validated and is detailed in Text S4. Solvation model based on density (SMD) was used to simulate the solvation interaction of molecules in water.[50-52]

In order to depict the molecular orbital (MO) interactions of these precursors, charge decomposition analysis (CDA) was conducted by Gaussian 16 and Multiwfn 3.8 dev.[53, 54] The radical precursors were deliberately divided into two open-shell fragments, and the geometry optimizations were calculated at UB3LYP-D3 functional in

197 combination with 6-31++G(d,p) basis set.[55] Then, the Gaussian output files for
198 precursors and fragments were imported to Multiwfn 3.8 dev., and the orbital
199 interaction diagram was plotted. Frontier orbital energies are used for the investigation
200 of photochemical reactions. In particular, the electron densities in the highest occupied
201 molecular orbital (HOMO) and lowest unoccupied molecular orbital (LUMO) were
202 used to interpret radical formation.[56] A compound with a small energy gap of HOMO
203 and LUMO is more susceptible to UV irradiation.
204
205 **3. RESULTS AND DISCUSSION**
206 **3.1 Formation kinetics of $^{\bullet}$OH by H_2O_2**
207 Figure 1a illustrates that with an increase of the initial concentration of SCN^-, the
208 maximal absorbance at 475 nm increased from 0.11 ([SCN^-] = 1 mM, blue line) to 0.14
209 ([SCN^-] = 5 mM, red line). The absorbance remained unchanged with further
210 concentration increase (red and green lines overlaps). This observation can be attributed
211 to the competitive reactions of $^{\bullet}$OH with SCN^- (eqn. 5) and H_2O_2 (eqn. 10).
212 $$^{\bullet}OH + H_2O_2 \rightarrow H_2O + HO_2^{\bullet} \quad (10)$$
213 von Sonntag proposed the concept of scavenging capacity,[57] and we calculated the
214 capacities for SCN^- and H_2O_2:
215 $$\text{scavenging capacity} = k \times [\text{scavenger}] \quad (11)$$
216 where k is the second-order reaction rate constant of a radical with a scavenger. With
217 the k values of 1.4×10^{10} and 2.7×10^7 $M^{-1}s^{-1}$ for SCN^- and H_2O_2, respectively,[20] the
218 scavenger capacity of SCN^- is 130 times higher than that of H_2O_2, demonstrating that
219 the resulting $^{\bullet}$OH in the photolysis of H_2O_2 was completely scavenged (> 99%) by SCN^-
220 at 5 mM. Note, the recombination of $^{\bullet}$OH can be another important sink, and this
221 reaction is also fast with a k value of 1.1×10^{10} M^{-1} s^{-1}.[46] However, this reaction is a

negligible sink of $^{\bullet}OH$ since the concentration of $^{\bullet}OH$ is significantly lower than that of SCN^{-}.

We monitored the absorption trace of $(SCN)_2^{\bullet-}$ at pH = 7 and [SCN^{-}] = 5 mM. As shown in Figure 1b, the maximum absorbance was 0.14. With the molar extinction coefficient (ε) of 7400 M^{-1} cm^{-1} for $(SCN)_2^{\bullet-}$,[38] its initial concentration was determined to be 19.4 μM (Figure S2), and the $N(^{\bullet}OH)_0$ was calculated to be 9.19×10^{15}. Since H_2O_2 solution only absorbs a fraction of photons, $N(h\nu)$ can be calculated as:

$$N(h\nu) = \frac{E\lambda}{hc} \times (1\text{-}T) = \frac{E\lambda}{hc} \times (1-10^{-Cb\varepsilon}) \quad (12)$$

where E refers to the laser energy per pulse and T refers to the transmittance of working solutions. The apparent $\varepsilon_{H_2O_2}$ at 266 nm was measured to be low at 7.2 M^{-1} cm^{-1} (Figure S3, a precursor with low ε value indicates that it exhibits weak absorption for UV, thus causing inefficient radical formation). Therefore with eqn. 4, the $\Phi_{\bullet OH}$ value was determined to be 1.10 ± 0.01.

Our value was in good agreement with the one measured by Goldstein *et al* (Table S2). They used methanol as a probe to measure $\Phi_{\bullet OH}$ in a UV/H_2O_2 system, as the generated $^{\bullet}OH$ reacts with methanol forming formaldehyde stoichiometrically. They quantitated formaldehyde *via* the addition of acetylacetone, and the adduct formed with a relatively high absorption. Based on the derivatization technique, $\Phi_{\bullet OH}$ was deduced to be 1.16 ± 0.05.[58] However, our $\Phi_{\bullet OH}$ value was about 10% higher than that by Yu *et al.* ($\Phi_{\bullet OH}$ = 1.0). They used Cl^{-} as a probe for $^{\bullet}OH$ (eqn. 13), as the formed $Cl_2^{\bullet-}$ (eqn. 14) can be observed through its characteristic absorption peak at 364 nm.[23]

$$^{\bullet}OH + Cl^{-} \rightarrow {}^{\bullet}Cl + OH^{-} \quad (13)$$

$$^{\bullet}Cl + Cl^{-} \leftrightarrow Cl_2^{\bullet-} \quad (14)$$

We believe that their method for $\Phi_{\bullet OH}$ exhibits a notable degree of uncertainty. In their

system, there exists 16 parallel/sequential reaction pathways, presenting an obstacle for extrapolation back to initial concentration of $Cl_2^{\bullet-}$. Many secondary/tertiary radical (*e.g.*, $ClO^{\bullet}$ and $HOCl^{\bullet-}$) and their interference on $Cl_2^{\bullet-}$ concentration were neglected for simplification, eventually resulting in a large, propagated error of $\Phi_{\bullet OH}$. In addition, the presence of $Cl_2^{\bullet-}$ is always accompanied by $Cl^{\bullet}$ (eqn. 14), and the spectra of $Cl_2^{\bullet-}$ and $Cl^{\bullet}$ overlap at the wavelength (364 nm) they monitored, adding another layer of complexity.[59] Note we did not observe any potential interference of SCN^- (Figure S4) and phosphate buffer (Figure S5) on $\Phi_{\bullet OH}$ determination (Text S5).

3.2 Formation kinetics of $SO_4^{\bullet-}$ by PDS

The detection of $SO_4^{\bullet-}$ was achieved by direct monitoring at its feature wavelength, 450 nm ($\varepsilon = 1650\ M^{-1}\ cm^{-1}$),[60] and $N(SO_4^{\bullet-})_0$ was derived from the maximum absorbance. Figure 1c (red line) showed that after the excitation, the maximal absorbance can increase to 0.044, and the initial concentration of produced $SO_4^{\bullet-}$ was then determined to be 26.6 μM (Figure 1c, inset red line). To quantify the number of photons $N(h\nu)$, the ε_{PDS} at 266 nm was measured to be 7.5 $M^{-1}cm^{-1}$ (Figure S3). With eqn. 4, $\Phi_{SO_4^{\bullet-}}$ was measured to be 1.46 ± 0.05. Note, we also conducted direct photolysis of phosphate buffer and monitored its kinetic decay at 450 nm. No diagnostic absorbance change was observed (Figure S5b), thus phosphate buffer exerts no effect on $\Phi_{SO_4^{\bullet-}}$ determinations.

Our $SO_4^{\bullet-}$ result is close to the value reported by Gertraud *et al.* ($\Phi_{SO_4^{\bullet-}} = 1.4$, Table S2). They investigated the photolysis of PDS at 254 nm in deoxygenated solutions.[61] In the presence of *tert*-butanol (TBA, a hydrogen donor), $SO_4^{\bullet-}$ reacts with TBA forming a stoichiometric number of protons, and this process can be followed by measuring the pH change *in situ*. It should be noted that as a macroscopic measure of solutions, pH cannot provide a direct indication of the radical concentration.

Interestingly, many studies simply proposed that $\Phi_{SO_4^{\bullet-}}$ is equal to 2 (similar to $\Phi_{\bullet OH}$ from H_2O_2), since one PDS molecule absorbs a photon for O-O bond fission and subsequently two $SO_4^{\bullet-}$ molecules are produced.[22, 62] This statement might be true in gas phase. However, $\Phi_{SO_4^{\bullet-}}$ in aqueous solution is often significantly lower due to the solvent cage effect.[63] When two $SO_4^{\bullet-}$ are formed simultaneously in the neighboring micro-environment before diffusing into bulk, they tend to recombine due to limited diffusion processes, resulting in heat release, but no net reaction.

In addition to direct detection of $SO_4^{\bullet-}$, we also used SCN^- as a probe for determining $\Phi_{SO_4^{\bullet-}}$ *via* monitoring the absorption trace of $SCN_2^{\bullet-}$ at 475 nm. Redpath *et al.* measured the *k* value of $SO_4^{\bullet-}$ with SCN^- through pulse radiolysis. They proposed the product can be assigned to $SCN_2^{\bullet-}$ based on transient spectra obtained after 1 krad pulse.[64] Similar to the scavenging capacity analysis in the H_2O_2 system, the reactions of $SO_4^{\bullet-}$ with other matrix constitutes (*i.e.,* PDS, H_2O and phosphate buffer, eqn.15-17)[65] can be neglected in the presence of SCN^-, and we concluded that $SO_4^{\bullet-}$ was completely scavenged by SCN^-.

$$SO_4^{\bullet-} + S_2O_8^{2-} \rightarrow S_2O_8^{\bullet-} + SO_4^{2-} \quad (15)$$

$$SO_4^{\bullet-} + H_2O \rightarrow HSO_4^- + {}^{\bullet}OH \quad (16)$$

$$SO_4^{\bullet-} + H_2PO_4^- \rightarrow SO_4^{2-} + H_2PO_4^{\bullet} \quad (17)$$

As shown in Figure 1c (blue line), the maximum absorbance spiked to 0.19. The initial concentration of $SCN_2^{\bullet-}$ was measured to be 26 μM (Figure 1c, inset blue line). With the stoichiometric ratio, the initial concentration of $SO_4^{\bullet-}$ was also determined to be 26 μM, ultimately the $\Phi_{SO_4^{\bullet-}}$ was calculated to be 1.40 *via* eqn. 4. This result is in excellent agreement with the value by our direct detection, corroborating the robustness of our time-resolved technique.

295

296 **3.3 Formation kinetics of $SO_4^{\bullet-}$ and $^{\bullet}OH$ by PMS**

297 PMS is also an efficient precursor for $SO_4^{\bullet-}$, and it is widely used for the
298 degradation of micropollutants in engineered water treatment systems.[66, 67] We
299 measured $\Phi_{SO_4^{\bullet-}}$ from the photolysis of PMS. The absorption traces of $SO_4^{\bullet-}$ at 450 nm
300 were recorded, and an intense maximum absorption reached up to 0.017 (Figure 1d).
301 Thus, the initial concentration of $SO_4^{\bullet-}$ was calculated to be 10.4 μM (Figure S6). With
302 ε_{PMS} at 266 nm being 7.8 $M^{-1}cm^{-1}$ (Figure S3), $\Phi_{SO_4^{\bullet-}}$ was measured to be 0.57 ± 0.02.
303 This value is in an agreement with a previous reported value (Table S2). Guan *et al.*
304 calculated $\Phi_{SO_4^{\bullet-}}$ produced from PMS irradiation by means of competition kinetics in a
305 steady-state system. They used nitrobenzene and benzoic acid as probes for $^{\bullet}OH$ and
306 $SO_4^{\bullet-}$, respectively. The $\Phi_{SO_4^{\bullet-}}$ was measured to be 0.52 by subtracting the contribution
307 of $^{\bullet}OH$.[68] However, our result was significantly higher than the value by Herrmann
308 (0.12 ± 0.02).[69] Their measurement was conducted assuming that the major sink for
309 $SO_4^{\bullet-}$ is its self-recombination, and he only considered this reaction to derive (calculate)
310 back to the initial concentration of $SO_4^{\bullet-}$, thus the $\Phi_{SO_4^{\bullet-}}$ was seriously underestimated.
311 However, the decay of $SO_4^{\bullet-}$ undergoes a series of parallel and consecutive reactions in
312 aqueous solution.[68] Neglecting these side reactions leads to an underestimation of
313 $\Phi_{SO_4^{\bullet-}}$.

314 In addition to $SO_4^{\bullet-}$, PMS also generates $^{\bullet}OH$ through the cleavage of the peroxy
315 bond, and the resulting $^{\bullet}OH$ can trigger the degradation of micropollutants in radical-
316 based treatment processes.[70, 71] Figure S7 demonstrates the commonly-used probe
317 SCN^- cannot be used in the PMS system because these two compounds react rapidly.[72]
318 Therefore, we developed a new approach to determine $\Phi_{^{\bullet}OH}$ in the PMS system using
319 TPA, a compound exhibiting low reactivity with PMS due to the presence of electron

withdrawing group. We measured the full absorption spectrum of the working solution containing TPA and PMS. As demonstrated in Figure S8, a distinct negative absorption (emission) from 330 to 360 nm is observed, but this band undergoes complete recovery within 60 ns. This observation indicated that one or more new species were formed at the early delay time before the formation of the more stable product. Subsequently, a negative absorption band due to the formation of hTPA (eqn. 8) emerges. This assignment was supported by the fluorescence spectra in this region at steady-state (Figure S9). Therefore, 60 ns after excitation was chosen as the baseline (time zero) for the event of hTPA formation.

As illustrated in Figure 2a (blue lines), the absorption signal went negative in the 400-600 nm region. The negative absorption almost completely recovers within 54 ns, and its lifetime on nanosecond timescale also confirmed the fluorescence emission of hTPA. The initial absorbance (ΔA_{total}) at 450 nm was selected, and it was measured to be –0.14. The ΔA_{total} value could be potentially due to the concurrent spectroscopic contribution from TPA, $SO_4^{\bullet-}$, and hTPA. Therefore, each part was profiled in the control experiments. The full transient absorption spectrum of TPA was measured (Figure 2a, green lines), and its initial absorbance at 450 nm (ΔA_{TPA}) is –0.083. Similarly, the full absorption spectrum for the mixed solution of TPA and PDS was scanned (Figure 2a purple lines), showing that its initial absorbance at 450 nm ($\Delta A_{SO_4^{\bullet-}}$) is –0.038. Therefore, the residual negative absorbance resulting from the formation of hTPA (ΔA_{hTPA}) can be back-calculated:

$$\Delta A_{\text{hTPA}} = \Delta A_{\text{total}} - \Delta A_{\text{TPA}} - f \times \Delta A_{SO_4^{\bullet-}} \quad (18)$$

where f is the ratio of the initial concentration of $SO_4^{\bullet-}$ produced from PMS (10.4 μM) to that from PDS (26.6 μM). The ΔA_{hTPA} value of –0.042 by eqn. 18 provided convincing evidence that $^{\bullet}OH$ is generated from the photolysis of PMS.

Note, the resultant absorption difference between ΔA_{TPA} and $\Delta A_{SO_4^{\bullet-}}$ may be attributed to the generated $SO_4^{\bullet-}$. (*i*) $SO_4^{\bullet-}$ exhibits significant absorption at 450 nm, that could offset the negative absorbance; (*ii*) $SO_4^{\bullet-}$ reacts with TPA with a *k* value of 1.7×10^8 $M^{-1}s^{-1}$,[73] decreasing the concentration of TPA. But these spectroscopic interferences were excluded *via* eqn. 18.

To quantify the formed hTPA, a calibration of standard hTPA solutions was performed (Figure S10). Figure 2b shows that with an increase of concentration of hTPA from 1 to 20 μM, the ΔA_{hTPA} value at 450 nm decreases from −0.014 to −0.025. With the calibration, the initial concentration of hTPA in the PMS system was determined to be 3.11 μM. Thus, the initial concentration of •OH produced from PMS is calculated to be 10.3 μM based on the hTPA formation yield of 0.3.[74-76] With these inputs, the $\Phi_{\bullet OH}$ value was determined to be 0.56 *via* eqn. 4, which is stoichiometrically equal to $\Phi_{SO_4^{\bullet-}}$ (0.57 ± 0.02) in the same system.

Page *et al.* proposed that TPA was an unsuitable probe for the study of photochemical systems under UV irradiation with wavelength shorter than 360 nm,[42] as hTPA is less photostable than TPA. The indication holds in a steady-state system. However, in non-steady state, the working solution was fully replenished by a peristaltic pump. Thus, our LFP system effectively decreased the exposure time of hTPA to UV irradiation, minimizing direct photolysis of hTPA. This is the first study to directly measure $\Phi_{\bullet OH}$ from the photolysis of PMS, exhibiting the competence of TPA as a probe in non-steady state systems.

Note, based on the full absorption spectrum of 10 μM hTPA (Figure S11), a pronounced negative absorption band at 330 nm was observed and it gradually recovered to 0 within 84 ns (Figure S12). The result indicated that after excitation hTPA generates new species. However, we did not identify them, as the negative absorbance

at 450 nm was almost unchanged, and thus the formed species did not interfere with the fluorescence determination at our target wavelength.

3.4 Radical formation mechanisms

Although the selected precursors possess low ε values (*i.e.*, they are relatively weakly absorbing) at 266 nm, they exhibit different capacities to form radicals. In this section we used the bond dissociation enthalpy (BDE) of the peroxy bond (O–O) and the HOMO shape to elucidate radical formation mechanisms. The BDE values of the peroxy bond for H_2O_2, PDS and PMS were calculated as 47.0, 22.4, and 33.4 kcal mol^{-1}, respectively (Table S3). These values were all significantly lower than that of the irradiation energy (107.5 kcal mol^{-1}), showing the thermodynamic feasibility of radical formation. However, BDE values reflect the strength of the peroxy bond in the gas phase, and may not well represent the chemical processes in aqueous solutions.[77]

To shed light on radical formation mechanisms from an electronic structure perspective, the alpha orbital interaction diagrams and the frontier molecular orbitals of precursors were determined and compared (Figure 3). The contribution (blue digits) of fragment orbitals (FOs) to precursor orbitals were obtained *via* Mulliken analysis. For example, the alpha HOMO of H_2O_2 (Figure 3a) is constructed by mixing alpha FO 5 and FO 4 of two $^{\bullet}OH$ fragments, and each contributes 50% to H_2O_2 orbital formation. Based on their orbital shapes (Figure 3 lower panel), the HOMOs of these precursors are peroxy antibonding orbitals. These orbitals result from the out-of-phase combination of atomic orbitals, leading to a reduction in electron density and repulsive force in between.[78] Ultimately, the repulsion destabilizes the peroxy bond, facilitating its cleavage and the formation of radicals. The shapes of other orbitals of radicals and precursor see Table S4-S8.

Based on our measurement, the susceptibility of the selected precursors towards UV irradiation decreases in the following order: PDS > PMS > H_2O_2. The $\Phi_{SO_4^{\bullet-}}^{PDS}$ and $\Phi_{^{\bullet}OH}^{H_2O_2}$ values were measured to be 1.46 and 1.10, respectively. The $\Phi_{radical}^{PMS}$ value is determined to be 1.13 (*i.e.*, the sum of $\Phi_{SO_4^{\bullet-}}$ = 0.57 and $\Phi_{^{\bullet}OH}$ = 0.56). With similar and low ε values, this trend can be predominantly attributed to the quantity of radicals formed. We provided a set of thermodynamic parameters for qualitative comparison. The BDE value of H_2O_2 (47.0 kcal mol^{-1}) is the highest, indicating that the peroxy bond of H_2O_2 is the most difficult of the three precursors to be cleaved. Although kinetics and thermodynamics are not a *priori* connected, these calculated BDE results could reflect the trend of radical formation quantity. We also calculated bond length and Mayer bond order for a more holistic comparison of this particular bond (Table S3).[79] The O-O bond in PDS is the most thermodynamically favorable for the dissociation, as it exhibits the longest bond length (1.478 Å) and the lowest Mayer bond order (0.8785). In addition, the energy gaps of HOMO and LUMO (E_{gap}) of precursors were also considered. A larger E_{gap} implies high stability and low reactivity in chemical reactions. The E_{gap} value of PDS (6.73 eV) is lower than that of PMS (7.11 eV) and H_2O_2 (7.46 eV). After irradiation, a peripheral electron on HOMO is susceptible to transit to LUMO, ultimately being photolyzed from an unstable state. This indication was also in good agreement with those drawn from bond strength analysis.

4. ENVIRONMENTAL IMPLICATIONS

We developed a direct and accurate method for radical Φ determinations in non-steady state systems by the LFP technique and applied it to three representative precursors. For H_2O_2 and PDS, this method can achieve real-time visualization of short-lived radicals (*i.e.*, $^{\bullet}OH$ and $SO_4^{\bullet-}$), including excellent reproducibility. Our method

avoids additional steps such as chemical derivatization and analytical separation, reducing the operational complexity and error propagation. For PMS, we presented a new approach for •OH quantification using LFP with TPA as a trap-and-trigger probe. The successful implementation of TPA for the PMS system is possible because of the highly fluorescent product (hTPA) formed from the reaction of TPA and •OH,[41] and its high resistance to reaction with PMS.[72] It should be noted that, in traditional chemical probe work, a given aqueous sample might be studied multiple times, each time with a different probe to quantify a different oxidant.[80] To increase the selectivity of each probe, either a scavenger is added to the sample (*e.g.*, 2-propanol to suppress •OH) or the contributions of non-target oxidants are mathematically corrected for once their concentrations have been determined. The breakthrough we present here shows that LFP can be combined with probes to determine multiple oxidants in one system. For probe compounds, we expect that future work will expand this concept to many other probes. The spectroscopic specificity and selectivity of probe compounds should be taken into consideration. It is also anticipated that the probe is water soluble and exhibits low reactivity with radical precursors.

The efficiency of radical formation from UV irradiation of the selected precursors decreases in the following order: PDS ($\Phi_{SO_4^{\bullet-}}^{PDS}$ = 1.46) > PMS ($\Phi_{radical}^{PMS}$ = $\Phi_{SO_4^{\bullet-}}$ + $\Phi_{\bullet OH}$ = 1.13) > H_2O_2 ($\Phi_{\bullet OH}^{H_2O_2}$ = 1.10). This study can be used to evaluate the performance of various AOPs, facilitating the selection of the most suitable one in different treatment scenarios. With the similar ε values of these three precursors, radical Φ is proportional to the concentration of radicals, and the concentration of radicals is the one of the two factors (radical reactivity) determining the degradation kinetics of micropollutants. Based on our results, UV/PDS is the most efficient technology, as it can generate the most radicals. But for a more holistic evaluation of AOPs, other parameters such as pH,

total dissolved solids, and salinity should also be considered. In addition, our theoretical results showed that the HOMO of these precursors are the O-O antibonding orbitals, resulting in bond fission and facile radical formation. We also calculated other electronic structures of selected precursors and their thermodynamic properties, confirming that the experimental observations that PDS indeed is thermodynamically favored to dissociate for radical formation, while H_2O_2 is less photochemically labile.

ACKNOWLEDGEMENT

Funding from National Natural Science Foundation of China (No. 22376220 and 52121004) are acknowledged. C.A. was supported by the US National Science Foundation (No. 2220307).

ASSOCIATED CONTENT

Additional texts providing the detail information of chemical and reagent sources, H_2O_2 calibration, relationship of ΔA and $\Delta T/T$, validation of basis set, exclusion of interference of SCN^- and phosphate buffer, calculations of the bond dissociation enthalpies, comparison of radical quantum yields, orbital surface plots, schematic diagram of LFP, absorption spectra of precursors, absorption traces of $SCN_2^{\bullet-}$ and $SO_4^{\bullet-}$, photolysis of PMS in the presence of SCN^-, photolysis of TPA and PMS, fluorescence spectra of hTPA, absorption spectra of hTPA at different concentrations, plot of ΔA values as function of time.

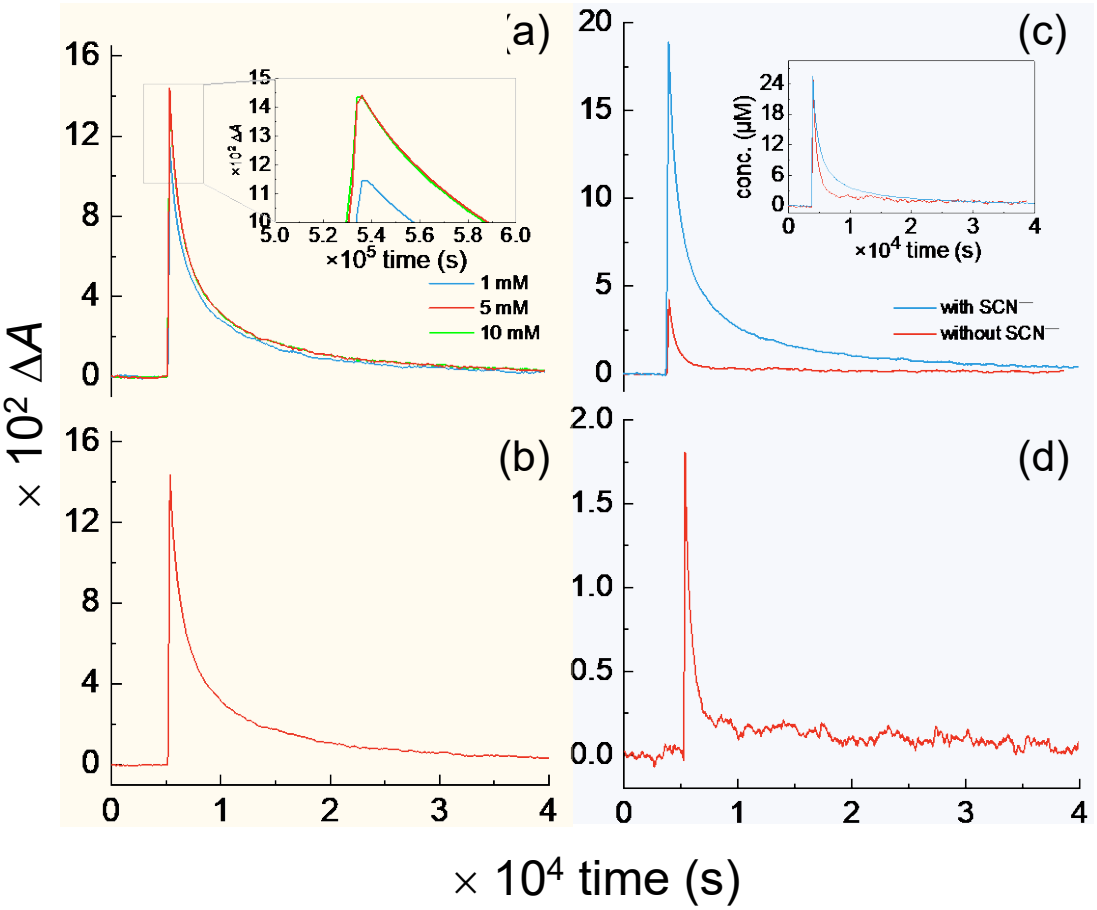

Figure 1: Laser flash photolysis of aqueous H_2O_2, PDS and PMS ([precursor] = 20 mM, [phosphate buffer] = 5 mM and pH = 7). (a) In the H_2O_2 system, comparison of absorption traces of $SCN_2^{\bullet-}$ with an increase of SCN^- concentration. The inset illustrates the magnified maximal absorbance region. (b) In the H_2O_2 system, absorption traces of $SCN_2^{\bullet-}$ in the presence of 5 mM SCN^-. (c) In the PDS system, comparison of absorption trace of $SO_4^{\bullet-}$ monitored at 450 nm (red) and $SCN_2^{\bullet-}$ monitored at 475 nm (blue). The inset corresponds to the concentration decay of $SO_4^{\bullet-}$ and $SCN_2^{\bullet-}$. Both traces demonstrate that the maximal concentrations of $SO_4^{\bullet-}$ in these systems are 26 μM ([SCN^-] = 1 mM). (d) In the PMS system, the absorption trace of $SO_4^{\bullet-}$ monitored at 450 nm.

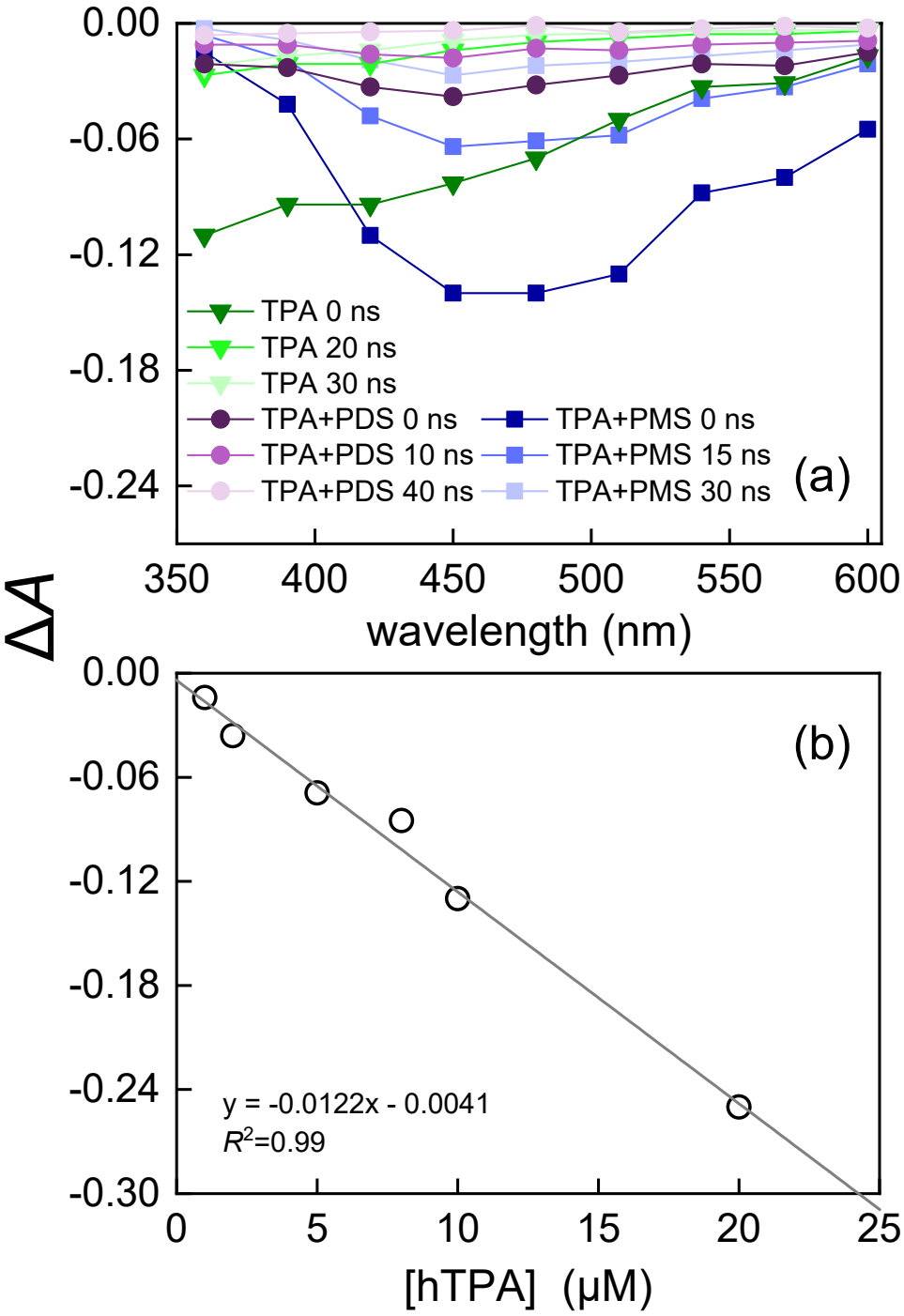

Figure 2: (a) The absorption spectra of different working solutions (TPA: green; TPA + PDS: purple; TPA + PMS: blue). They were scanned from 360 nm to 600 nm. ([TPA] = 5 mM, [PDS] = 20 mM, [PMS] = 20 mM, [phosphate buffer] = 5 mM, and pH =7.) (b) The plot of the ΔA value at the wavelength of 450 nm *vs*. hTPA concentrations ([hTPA] = 0~20 μM, [phosphate buffer] = 5 mM, and pH =7.)

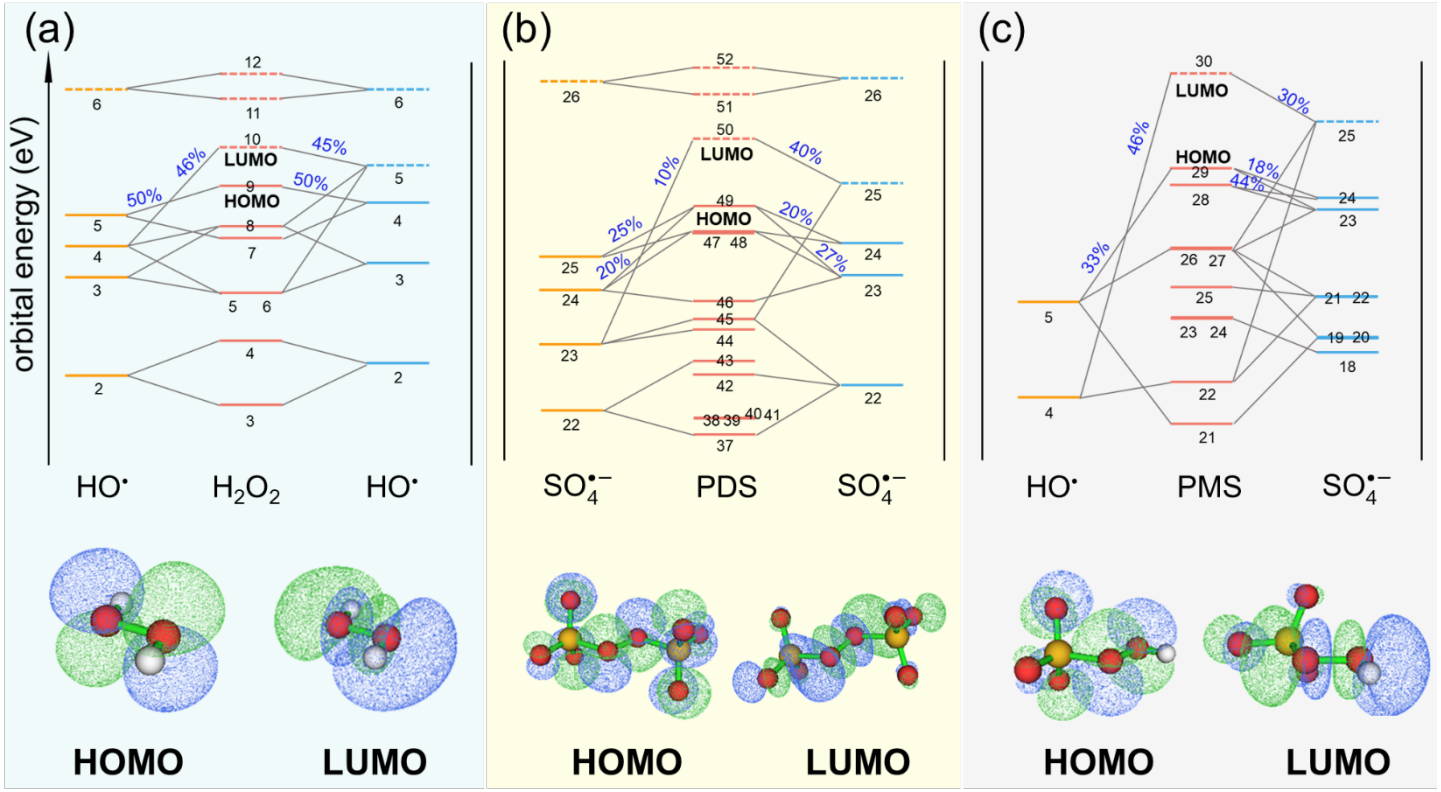

Figure 3: Alpha orbital interaction diagrams of H_2O_2 (a), PDS (b), and PMS (c). Red lines represent orbitals of the precursors, while yellow and blue lines for corresponding radical fragments. For all the radical precursors, solid and dashed lines denote occupied and unoccupied orbitals, respectively. Orbital indices are labelled by black texts. If two or more labels occur in the same line, that means these orbitals are degenerated in energy (*e.g.*, orbital 47 and 48 in PDS (b)). The blue numbers represent the component of the fragment orbital in their parent molecules. For example, the alpha HOMO of H_2O_2 (a) is constructed by mixing alpha fragment orbital (FO) 5 and FO 4 of two •OH fragments, and each contributes 50% to HOMO orbital formation. Orbital surface plots of HOMO and LUMO for each precursor were drawn with isodensity value of 0.02 e Bohr^{-3}.

REFERENCES

1. von Gunten, U., Oxidation processes in water treatment: Are we on track? *Environ. Sci. Technol.* **2018,** *52*, (9), 5062-5075.
2. Richardson, S. D.; Kimura, S. Y., Water analysis: Emerging contaminants and current issues. *Anal. Chem.* **2020,** *92*, (1), 473-505.
3. Westerhoff, P.; Yoon, Y.; Snyder, S.; Wert, E., Fate of Endocrine-Disruptor, Pharmaceutical, and Personal Care Product Chemicals during Simulated Drinking Water Treatment Processes. *Environ. Sci .Technol.* **2005,** *39*, (17), 6649-6663.
4. Keen, O. S.; Linden, K. G., Degradation of Antibiotic Activity during UV/H_2O_2 Advanced Oxidation and Photolysis in Wastewater Effluent. *Environ. Sci .Technol.* **2013,** *47*, (22), 13020-13030.
5. Min, X.; Chu, C.; Luo, Z.; Ma, J.; Fu, Y.; Wei, Z.; Spinney, R.; Dionysiou, D. D.; Xiao, R., Transformation of phenol and nitrobenzene by superoxide radicals: Kinetics and mechanisms. *Chem. Eng. J.* **2022,** *442*, 136134.
6. Zhang, T.; Huang, C.-H., Modeling the Kinetics of UV/Peracetic Acid Advanced Oxidation Process. *Environ. Sci .Technol.* **2020,** *54*, (12), 7579-7590.
7. Qu, R.; Li, C.; Liu, J.; Xiao, R.; Pan, X.; Zeng, X.; Wang, Z.; Wu, J., Hydroxyl Radical Based Photocatalytic Degradation of Halogenated Organic Contaminants and Paraffin on Silica Gel. *Environmental Science & Technology* **2018,** *52*, (13), 7220-7229.
8. Gao, L.; Minakata, D.; Wei, Z.; Spinney, R.; Dionysiou, D. D.; Tang, C.-J.; Chai, L.; Xiao, R., Mechanistic Study on the Role of Soluble Microbial Products in Sulfate Radical-Mediated Degradation of Pharmaceuticals. *Environ. Sci .Technol.* **2019,** *53*, (1), 342-353.
9. Wang, L.; Ye, C.; Guo, L.; Chen, C.; Kong, X.; Chen, Y.; Shu, L.; Wang, P.; Yu, X.; Fang, J., Assessment of the UV/Chlorine Process in the Disinfection of Pseudomonas aeruginosa: Efficiency and Mechanism. *Environ. Sci .Technol.* **2021,** *55*, (13), 9221-9230.
10. Sun, L.; Bolton, J. R., Determination of the Quantum Yield for the Photochemical Generation of Hydroxyl Radicals in TiO_2 Suspensions. *J. Phys. Chem.* **1996,** *100*, (10), 4127-4134.
11. Braslavsky, S. E., Glossary of terms used in photochemistry, 3rd edition (IUPAC Recommendations 2006). *Pure Appl. Chem.* **2007,** *79*, (3), 293-465.
12. Ho, T.-F. L.; Bolton, J. R.; Lipczynska-Kochany, E., Quantum Yields for the Photodegradation of Pollutants in Dilute Aqueous Solution: Phenol, 4-Chlorophenol and N-Nitrosodimethylamine. *J. Adv. Oxid. Technol.* **1996,** *1*, (2), 170-178.
13. Lee, W.; Lee, Y.; Allard, S.; Ra, J.; Han, S.; Lee, Y., Mechanistic and Kinetic Understanding of the UV254 Photolysis of Chlorine and Bromine Species in Water and Formation of Oxyhalides. *Environ. Sci .Technol.* **2020,** *54*, (18), 11546-11555.
14. Shao, H.; Chen, J.; Xu, J.; Liu, Y.; Dong, H.; Qiao, J.; Guan, X., Naproxen as a Turn-On Chemiluminescent Probe for Real-Time Quantification of Sulfate Radicals. *Environ. Sci. Technol.* **2023,** *57*, (23), 8818-8827.
15. Yang, Y.; Jiang, J.; Lu, X.; Ma, J.; Liu, Y., Production of sulfate radical and hydroxyl radical by reaction of ozone with peroxymonosulfate: a novel advanced oxidation process. *Environ. Sci. Technol.* **2015,** *49*, (12), 7330-9.

16. Chen, Y.; Miller, C. J.; Xie, J.; Waite, T. D., Challenges Relating to the Quantification of Ferryl(IV) Ion and Hydroxyl Radical Generation Rates Using Methyl Phenyl Sulfoxide (PMSO), Phthalhydrazide, and Benzoic Acid as Probe Compounds in the Homogeneous Fenton Reaction. *Environ. Sci .Technol.* **2023**.
17. Vione, D.; Ponzo, M.; Bagnus, D.; Maurino, V.; Minero, C.; Carlotti, M. E., Comparison of different probe molecules for the quantification of hydroxyl radicals in aqueous solution. *Environ. Chem. Lett.* **2010,** *8*, (1), 95-100.
18. Carlsson, C.; Fégeant, B.; Svensson, E.; Wiklund, L.; Jonsson, M., On the Selectivity of Radical Scavengers Used To Probe Hydroxyl Radical Formation in Heterogeneous Systems. *J. Phys. Chem. C* **2022,** *126*, (30), 12435-12440.
19. Zhou, X.; Mopper, K., Determination of photochemically produced hydroxyl radicals in seawater and freshwater. *Mar. Chem.* **1990,** *30*, 71-88.
20. Buxton, G. V.; Greenstock, C. L.; Helman, W. P.; Ross, A. B., Critical Review of rate constants for reactions of hydrated electrons, hydrogen atoms and hydroxyl radicals ($^{\bullet}OH/^{\bullet}O^{-}$) in Aqueous Solution. *J. Phys. Chem. Ref. Data* **1988,** *17*, (2), 513-886.
21. Treviño-Reséndez, J.; Medel, A.; Mijaylova, P.; Robles, I.; Rodríguez-Valadez, F.; Godínez, L. A.; Meas, Y., Insight into the generation of hydroxyl radicals by photo-electrocoagulation process via active chlorine. *Int. J. Environ. Sci. Technol.* **2022,** *19*, (4), 2913-2924.
22. Yu, X.-Y.; Bao, Z.-C.; Barker, J. R., Free Radical Reactions Involving $Cl^{\bullet}$, $Cl_2^{-\bullet}$, and $SO_4^{-\bullet}$ in the 248 nm Photolysis of Aqueous Solutions Containing $S_2O_8^{2-}$ and Cl. *J. Phys. Chem. A* **2004,** *108*, (2), 295-308.
23. Yu, X.-Y.; Barker, J. R., Hydrogen Peroxide Photolysis in Acidic Aqueous Solutions Containing Chloride Ions. II. Quantum Yield of $HO^{\bullet}$(Aq) Radicals. *J. Phys. Chem. A* **2003,** *107*, (9), 1325-1332.
24. Scaiano, J. C.; Selwyn, J. C., Triplet Energy Migration Between Carbonyl Chromophores In Micellar Solution. *Photochem. Photobiol.* **1981,** *34*, (1), 29-32.
25. Leresche, F.; Ludvíková, L.; Heger, D.; von Gunten, U.; Canonica, S., Quenching of an Aniline Radical Cation by Dissolved Organic Matter and Phenols: A Laser Flash Photolysis Study. *Environ. Sci .Technol.* **2020,** *54*, (23), 15057-15065.
26. Chu, C.; Yan, Y.; Ma, J.; Jin, S.; Spinney, R.; Dionysiou, D. D.; Zhang, H.; Xiao, R., Implementation of laser flash photolysis for radical-induced reactions and environmental implications. *Water Res.* **2023,** *244*, 120526.
27. Tong, X.; Wang, S.; Wang, L., Kinetics and mechanism of syringic acid degradation initiated by hydroxyl radical and sulphate radical in the aqueous phase. *Chemosphere* **2020,** *256*, 126997.
28. Lei, Y.; Lu, J.; Zhu, M.; Xie, J.; Peng, S.; Zhu, C., Radical chemistry of diethyl phthalate oxidation via UV/peroxymonosulfate process: Roles of primary and secondary radicals. *Chem. Eng. J.* **2020,** *379*, 122339.
29. Canonica, S.; Hellrung, B.; Müller, P.; Wirz, J., Aqueous Oxidation of Phenylurea Herbicides by Triplet Aromatic Ketones. *Environ. Sci .Technol.* **2006,** *40*, (21), 6636-6641.
30. Wenk, J.; Eustis, S. N.; McNeill, K.; Canonica, S., Quenching of Excited Triplet States by Dissolved Natural Organic Matter. *Environ. Sci .Technol.* **2013,** *47*, (22),

12802-12810.
31. Remke, S. C.; Burgin, T. H.; Ludvikova, L.; Heger, D.; Wenger, O. S.; von Gunten, U.; Canonica, S., Photochemical oxidation of phenols and anilines mediated by phenoxyl radicals in aqueous solution. *Water Res.* **2022,** *213*, 118095.
32. El Omar, A. K.; Schmidhammer, U.; Jeunesse, P.; Larbre, J. P.; Lin, M.; Muroya, Y.; Katsumura, Y.; Pernot, P.; Mostafavi, M., Time-dependent radiolytic yield of OH• radical studied by picosecond pulse radiolysis. *J. Phys. Chem. A* **2011,** *115*, (44), 12212-6.
33. Kobayashi, K., Pulse Radiolysis Studies for Mechanism in Biochemical Redox Reactions. *Chem. Rev.* **2019,** *119*, (6), 4413-4462.
34. Luo, S.; Gao, L.; Wei, Z.; Spinney, R.; Dionysiou, D. D.; Hu, W.-P.; Chai, L.; Xiao, R., Kinetic and mechanistic aspects of hydroxyl radical–mediated degradation of naproxen and reaction intermediates. *Water Res.* **2018,** *137*, 233-241.
35. Yan, Y.; Wei, Z.; Duan, X.; Long, M.; Spinney, R.; Dionysiou, D. D.; Xiao, R.; Alvarez, P. J. J., Merits and Limitations of Radical vs. Nonradical Pathways in Persulfate-Based Advanced Oxidation Processes. *Environ. Sci .Technol.* **2023**.
36. Zuo, Z.; Katsumura, Y.; Ueda, K.; Ishigure, K., Laser photolysis study on reactions of sulfate radical and nitrate radical with chlorate ion in aqueous solutions Formation and reduction potential of ClO_3 radical. *J. Chem. Soc., Faraday Trans.* **1997,** *93*, (4), 533-536.
37. Gligorovski, S.; Strekowski, R.; Barbati, S.; Vione, D., Environmental Implications of Hydroxyl Radicals (•OH). *Chem. Rev.* **2015,** *115*, (24), 13051-13092.
38. Milosavljevic, B. H.; LaVerne, J. A., Pulse Radiolysis of Aqueous Thiocyanate Solution. *J. Phys. Chem. A* **2005,** *109*, (1), 165-168.
39. Song, W.; O'Shea, K. E., Ultrasonically induced degradation of 2-methylisoborneol and geosmin. *Water Res.* **2007,** *41*, (12), 2672-2678.
40. Villeneuve, L.; Alberti, L.; Steghens, J. P.; Lancelin, J. M.; Mestas, J. L., Assay of hydroxyl radicals generated by focused ultrasound. *Ultrason. Sonochem.* **2009,** *16*, (3), 339-344.
41. nyrychová, I.; Hideg, É., The first application of terephthalate fluorescence for highly selective detection of hydroxyl radicals in thylakoid membranes. *Funct. Plant Biol.* **2007,** *34*, (12), 1105-1111.
42. Page, S. E.; Arnold, W. A.; McNeill, K., Terephthalate as a probe for photochemically generated hydroxyl radical. *J. Environ. Monit.* **2010,** *12*, (9), 1658-65.
43. Frisch, M. J.; Trucks, G. W.; Schlegel, H. B.; Scuseria, G. E.; Robb, M. A.; Cheeseman, J. R.; Scalmani, G.; Barone, V.; Petersson, G. A.; Nakatsuji, H.; Li, X.; Caricato, M.; Marenich, A. V.; Bloino, J.; Janesko, B. G.; Gomperts, R.; Mennucci, B.; Hratchian, H. P.; Ortiz, J. V.; Izmaylov, A. F.; Sonnenberg, J. L.; Williams; Ding, F.; Lipparini, F.; Egidi, F.; Goings, J.; Peng, B.; Petrone, A.; Henderson, T.; Ranasinghe, D.; Zakrzewski, V. G.; Gao, J.; Rega, N.; Zheng, G.; Liang, W.; Hada, M.; Ehara, M.; Toyota, K.; Fukuda, R.; Hasegawa, J.; Ishida, M.; Nakajima, T.; Honda, Y.; Kitao, O.; Nakai, H.; Vreven, T.; Throssell, K.; Montgomery Jr., J. A.; Peralta, J. E.; Ogliaro, F.; Bearpark, M. J.; Heyd, J. J.; Brothers, E. N.; Kudin, K. N.; Staroverov, V. N.; Keith, T. A.; Kobayashi, R.; Normand, J.; Raghavachari, K.; Rendell, A. P.; Burant, J. C.; Iyengar,

S. S.; Tomasi, J.; Cossi, M.; Millam, J. M.; Klene, M.; Adamo, C.; Cammi, R.; Ochterski, J. W.; Martin, R. L.; Morokuma, K.; Farkas, O.; Foresman, J. B.; Fox, D. J. *Gaussian 16 Rev. A.03*, Wallingford, CT, 2016.
44. Xiong, X.; Shang, Y.; Bai, L.; Luo, S.; Seviour, T. W.; Guo, Z.; Ottosen, L. D. M.; Wei, Z., Complete defluorination of perfluorooctanoic acid (PFOA) by ultrasonic pyrolysis towards zero fluoro-pollution. *Water Res.* **2023,** *235*, 119829.
45. Liu, J.; Van Hoomissen, D. J.; Liu, T.; Maizel, A.; Huo, X.; Fernández, S. R.; Ren, C.; Xiao, X.; Fang, Y.; Schaefer, C. E.; Higgins, C. P.; Vyas, S.; Strathmann, T. J., Reductive Defluorination of Branched Per- and Polyfluoroalkyl Substances with Cobalt Complex Catalysts. *Environ. Sci .Technol. Lett.* **2018,** *5*, (5), 289-294.
46. Wright *, J. S.; Rowley, C. N.; Chepelev, L. L., A 'universal' B3LYP-based method for gas-phase molecular properties: bond dissociation enthalpy, ionization potential, electron and proton affinity and gas-phase acidity. *Mol. Phys.* **2005,** *103*, (6-8), 815-823.
47. Klein, E.; Lukeš, V., DFT/B3LYP Study of the Substituent Effect on the Reaction Enthalpies of the Individual Steps of Single Electron Transfer−Proton Transfer and Sequential Proton Loss Electron Transfer Mechanisms of Phenols Antioxidant Action. *J. Phys. Chem. A* **2006,** *110*, (44), 12312-12320.
48. Grimme, S.; Antony, J.; Ehrlich, S.; Krieg, H., A consistent and accurate ab initio parametrization of density functional dispersion correction (DFT-D) for the 94 elements H-Pu. *J. Chem. Phys.* **2010,** *132*, (15), 154104.
49. Blanksby, S. J.; Ellison, G. B., Bond Dissociation Energies of Organic Molecules. *Acc. Chem. Res.* **2003,** *36*, (4), 255-263.
50. Marenich, A. V.; Cramer, C. J.; Truhlar, D. G., Universal Solvation Model Based on Solute Electron Density and on a Continuum Model of the Solvent Defined by the Bulk Dielectric Constant and Atomic Surface Tensions. *J. Phys. Chem. B* **2009,** *113*, (18), 6378-6396.
51. Galano, A.; Alvarez-Idaboy, J. R., Kinetics of radical-molecule reactions in aqueous solution: A benchmark study of the performance of density functional methods. *J. Comput. Chem.* **2014,** *35*, (28), 2019-2026.
52. Fu, Y.; Yan, Y.; Wei, Z.; Spinney, R.; Dionysiou, D. D.; Vione, D.; Liu, M.; Xiao, R., Overlooked Transformation of Nitrated Polycyclic Aromatic Hydrocarbons in Natural Waters: Role of Self-Photosensitization. *Environ. Sci .Technol.* **2023,** *57*, (26), 9832-9842.
53. Lu, T.; Chen, F., Multiwfn: A multifunctional wavefunction analyzer. *J. Comput. Chem.* **2012,** *33*, (5), 580-592.
54. Xiao, M.; Lu, T., Generalized Charge Decomposition Analysis (GCDA) Method. *Journal of Advances in Physical Chemistry* **2015,** *04*, (04), 111-124.
55. Kemnitz, C. R.; Squires, R. R.; Borden, W. T., Ab Initio Calculations on 1,3,5-Trimethylenebenzene and Its Negative Ion Provide Predictions about the Photoelectron Spectrum of the Ion. *J. Am. Chem. Soc.* **1997,** *119*, (28), 6564-6574.
56. Karelson, M.; Lobanov, V. S.; Katritzky, A. R., Quantum-Chemical Descriptors in QSAR/QSPR Studies. *Chem. Rev.* **1996,** *96*, (3), 1027-1044.
57. Mark, G.; Tauber, A.; Laupert, R.; Schuchmann, H.-P.; Schulz, D.; Mues, A.; von

669 Sonntag, C., OH-radical formation by ultrasound in aqueous solution – Part II:
670 Terephthalate and Fricke dosimetry and the influence of various conditions on the
671 sonolytic yield. *Ultrason. Sonochem.* **1998,** *5*, (2), 41-52.
672 58. Goldstein, S.; Aschengrau, D.; Diamant, Y.; Rabani, J., Photolysis of Aqueous
673 H_2O_2: Quantum Yield and Applications for Polychromatic UV Actinometry in
674 Photoreactors. *Environ. Sci .Technol.* **2007,** *41*, (21), 7486-7490.
675 59. Lei, Y.; Cheng, S.; Luo, N.; Yang, X.; An, T., Rate Constants and Mechanisms of
676 the Reactions of $Cl^{\bullet}$ and $Cl_2^{\bullet-}$ with Trace Organic Contaminants. *Environmental Science*
677 *& Technology* **2019,** *53*, (19), 11170-11182.
678 60. Zhu, Y.; Zhu, M.; Xie, J.; Hu, Y.; Liu, Y.; Zhu, C., Photochemical reaction kinetics
679 and mechanism of bisphenol A with $K_2S_2O_8$ in aqueous solution: a laser flash photolysis
680 study. *Can. J. Chem.* **2021,** *99*, (1), 43-50.
681 61. Mark, G.; Schuchmann, M. N.; Schuchmann, H.-P.; von Sonntag, C., The
682 photolysis of potassium peroxodisulphate in aqueous solution in the presence of *tert*-
683 butanol: a simple actinometer for 254 nm radiation. *J. Photochem. Photobiol. A: Chem.*
684 **1990,** *55*, (2), 157-168.
685 62. Tang, Y.; Thorn, R. P.; Mauldin, R. L.; Wine, P. H., Kinetics and spectroscopy of
686 the SO_4^- radical in aqueous solution. *J. Photochem. Photobiol. A: Chem.* **1988,** *44*, (3),
687 243-258.
688 63. Herk, L.; Feld, M.; Szwarc, M., Studies of "Cage" Reactions. *J. Am. Chem. Soc.*
689 **1961,** *83*, (14), 2998-3005.
690 64. Redpath, J. L.; Willson, R. L., Chain Reactions and Radiosensitization: Model
691 Enzyme Studies. *Int. J. Radiat. Biol.* **1975,** *27*, (4), 389-398.
692 65. Fang, G.-D.; Dionysiou, D. D.; Wang, Y.; Al-Abed, S. R.; Zhou, D.-M., Sulfate
693 radical-based degradation of polychlorinated biphenyls: Effects of chloride ion and
694 reaction kinetics. *J. Hazard. Mater.* **2012,** *227-228*, 394-401.
695 66. Yang, S.; Wang, P.; Yang, X.; Shan, L.; Zhang, W.; Shao, X.; Niu, R., Degradation
696 efficiencies of azo dye Acid Orange 7 by the interaction of heat, UV and anions with
697 common oxidants: Persulfate, peroxymonosulfate and hydrogen peroxide. *J. Hazard.*
698 *Mater.* **2010,** *179*, (1), 552-558.
699 67. Liu, X.; Zhang, T.; Zhou, Y.; Fang, L.; Shao, Y., Degradation of atenolol by
700 UV/peroxymonosulfate: Kinetics, effect of operational parameters and mechanism.
701 *Chemosphere* **2013,** *93*, (11), 2717-2724.
702 68. Guan, Y. H.; Ma, J.; Li, X. C.; Fang, J. Y.; Chen, L. W., Influence of pH on the
703 formation of sulfate and hydroxyl radicals in the UV/peroxymonosulfate system.
704 *Environ. Sci. Technol.* **2011,** *45*, (21), 9308-14.
705 69. Herrmann, H., On the photolysis of simple anions and neutral molecules as sources
706 of O^-/OH, SO_x^- and Cl in aqueous solution. *Phys. Chem. Chem. Phys.* **2007,** *9*, (30),
707 3935-3964.
708 70. Peng, Y.; Shi, H.; Wang, Z.; Fu, Y.; Liu, Y., Kinetics and reaction mechanism of
709 photochemical degradation of diclofenac by UV-activated peroxymonosulfate. *RSC*
710 *Adv.* **2021,** *11*, (12), 6804-6817.
711 71. Verma, S.; Nakamura, S.; Sillanpää, M., Application of UV-C LED activated PMS
712 for the degradation of anatoxin-a. *Chem. Eng. J.* **2016,** *284*, 122-129.

72. Lee, J.; von Gunten, U.; Kim, J. H., Persulfate-based advanced oxidation: critical assessment of opportunities and roadblocks. *Environ. Sci .Technol.* **2020,** *54*, (6), 3064-3081.
73. Neta, P.; Madhavan, V.; Zemel, H.; Fessenden, R. W., Rate constants and mechanism of reaction of sulfate radical anion with aromatic compounds. *J. Am. Chem. Soc.* **1977,** *99*, (1), 163-164.
74. Gonzalez, D. H.; Kuang, X. M.; Scott, J. A.; Rocha, G. O.; Paulson, S. E., Terephthalate Probe for Hydroxyl Radicals: Yield of 2-Hydroxyterephthalic Acid and Transition Metal Interference. *Anal. Lett.* **2018,** *51*, (15), 2488-2497.
75. Charbouillot, T.; Brigante, M.; Mailhot, G.; Maddigapu, P. R.; Minero, C.; Vione, D., Performance and selectivity of the terephthalic acid probe for OH as a function of temperature, pH and composition of atmospherically relevant aqueous media. *J. Photochem. Photobiol. A: Chem.* **2011,** *222*, (1), 70-76.
76. Tafer, R.; Sleiman, M.; Boulkamh, A.; Richard, C., Photomineralization of aqueous salicylic acids. Photoproducts characterization and formation of light induced secondary OH precursors (LIS-OH). *Water Res.* **2016,** *106*, 496-506.
77. Greenberg, A.; Green, A. R.; Liebman, J. F., Computational Study of Selected Amine and Lactam N-Oxides Including Comparisons of N-O Bond Dissociation Enthalpies with Those of Pyridine N-Oxides. *Molecules* **2020,** *25*, (16).
78. Ouellette, R. J.; Rawn, J. D., 1 - Structure and Bonding in Organic Compounds. In *Organic Chemistry*, Ouellette, R. J.; Rawn, J. D., Eds. Elsevier: Boston, 2014; pp 1-39.
79. Bridgeman, A.; Cavigliasso, G.; Ireland, L.; Rothery, J., The Mayer bond order as a tool in inorganic chemistry†. *J. Chem. Soc. Dalton Trans.* **2001,** *2001*, 2095-2108.
80. Rosario-Ortiz, F. L.; Canonica, S., Probe Compounds to Assess the Photochemical Activity of Dissolved Organic Matter. *Environ. Sci .Technol.* **2016,** *50*, (23), 12532-12547.

Trap-and-trigger determination of absolute radical quantum yields in radical-based treatment processes

Supporting information

Yiqi Yan[1, 2], Yunxiang Meng[1, 2], Kanying Miao[1, 2], Jannis Wenk[3], Cort Anastasio[4], Richard Spinney[5], Chong-Jian Tang[1, 2, *] and Ruiyang Xiao [1, 2, *]

[1] Institute of Environmental Engineering, School of Metallurgy and Environment, Central South University, Changsha, 410083, China

[2] Chinese National Engineering Research Center for Control & Treatment of Heavy Metal Pollution, Changsha, 410083, China

[3] Department of Chemical Engineering, Water Innovation & Research Centre (WIRC@Bath), University of Bath, BA2 7AY, UK

[4] Department of Land, Air, and Water Resource, University of California, Davis, California 95616, United States

[5] Department of Chemistry and Biochemistry, the Ohio State University, Columbus, Ohio, 43210, U.S.

*To whom correspondence should be addressed. C.J. Tang, Phone: +86–731–88830511, Email: chjtang@csu.edu.cn; R.X. Phone: +86–731–88830875, Email address: xiao.53@csu.edu.cn

Number of page for the supplementary imformation: 29

Number of texts: 5

Number of tables: 8

Number of figures: 12

Table of Contents

Text S1: Source of chemicals and reagents.

Potassium peroxydisulfate (PDS, Aladdin, 99.5%), potassium peroxymonosulfate (PMS, AR, Aladdin), terephthalic acid (TPA, Sigma–Alrich, 99%), hydroxyterephthalic acid (hTAP, Aladdin, ≥ 98%), potassium dihydrogen phosphate (KH_2PO_4, Sigma–Alrich, 99%), dibasic potassium phosphate (K_2HPO_4, Sigma–Alrich, 99.0%), potassium thiocyanate (KSCN, Sigma–Alrich, 99.0%), and sodium oxalate ($Na_2C_2O_4$, Sigma–Alrich, 99.0%) were used without further purification. Hydrogen peroxide (H_2O_2, *ca.* 30% by weight), and potassium permanganate ($KMnO_4$, AR) was purchased from Aladdin (Shanghai, China).

H_2O_2 was used as the precursor for $^{\bullet}OH$, while PDS is the $SO_4^{\bullet-}$ precursor. PMS was used as the precursor for both $^{\bullet}OH$ and $SO_4^{\bullet-}$. The concentration of H_2O_2 in this study was calibrated by $KMnO_4$ titration, and $Na_2C_2O_4$ was then used to determine the concentration of $KMnO_4$.[1] SCN^- was used as a probe for $^{\bullet}OH$ in the H_2O_2 system and TPA was used in the PMS system. Phosphate buffer solution (consisting of KH_2PO_4 and K_2HPO_4) was used to control solution pH at 7. The selection of a neutral pH was simply due to its environmental relevance. Experiments were performed at room temperature.

Text S2: The calibration of H_2O_2 concentration

H_2O_2 typically decomposes at the rate of approximately 0.5% per year at room temperature.[2] Thus, the H_2O_2 stock solution (*ca.* 30% by weight) was stored at 4 ℃ and regularly calibrated by titration. Specifically, the H_2O_2 concenration was measured by adding $KMnO_4$ to produce Mn^{2+} in an acidic condition[1]:

$$5H_2O_2 + 2MnO_4^- + 6H^+ \rightarrow 2Mn^{2+} + 8H_2O + 5O_2 \quad \text{(S1)}$$

The solution turned red and maintained the hue within 30 s, which was considered to be the endpoint of titration. It should be noted that $KMnO_4$ is a strong oxidant, and often contains impurities, thus it cannot be directly prepared for standard solution. We boiled $KMnO_4$ solution for 1 hr, and filtered the solution through a sand core funnel. Then, sodium oxalate ($Na_2C_2O_4$) was used to titrate $KMnO_4$ solution in an acidic condition (eqn. S2).[3] During this titration process, the temperature of the solution should be kept at least 60 ℃, but not above, as $C_2O_4^{2-}$ can self-decompose.

$$5C_2O_4^{2-} + 2MnO_4^- + 16H^+ \rightarrow 10CO_2 + 2Mn^{2+} + 8H_2O \quad \text{(S2)}$$

Text S3: The relationship of ΔA and $\Delta T/T$.

According to Lambert-Beer Law, the absorption (A) of a sample at a specific wavelength can be calculated as[4]:

$$A = -\log\frac{I_1}{I_0} = \varepsilon C\mathrm{b} \tag{S3}$$

where I_0 and I_1 represents the intensity of incident light and transmitted light, respectively. Thus, the absorption change (ΔA) before and after sample excitation by pump laser can be inferred to be:

$$\Delta A = A_{\text{pump}} - A_{\text{unpump}} = -\log\frac{I_{1\text{-pump}}}{I_{0\text{-pump}}} - (-\log\frac{I_{1\text{-unpump}}}{I_{0\text{-unpump}}}) = -\log\frac{I_{1\text{-pump}}}{I_{1\text{-unpump}}} \tag{S4}$$

where A_{pump} refers to the absorption of working solution after excitation, while $\mathrm{A}_{\text{unpump}}$ is for a sample before excitation. $I_{0\text{-pump}}$ and $I_{1\text{-pump}}$ represent the intensities of incident and transmitted light of the excited sample. $I_{0\text{-unpump}}$ and $I_{1\text{-unpump}}$ are the intensities of the incident and transmitted light in solutions without excitation. It should be noted that $I_{0\text{-pump}}$ is equal to $I_{0\text{-unpump}}$. Alternatively, relative transmittance ($\Delta T/T$) can be also used to reflect transient absorption signal:

$$\Delta T/T = \frac{I_{1\text{-pump}} - I_{1\text{-unpump}}}{I_{1\text{-unpump}}} = \frac{I_{1\text{-pump}}}{I_{1\text{-unpump}}} - 1 = 10^{-\Delta A} - 1 \tag{S5}$$

When ΔA is far less than 1, $\Delta T/T \approx -2.303\Delta A$, indicating an inverse correlation between $\Delta T/T$ and ΔA.

Text S4: Validation of 6-311G (2d, 2p) basis set.

To test against the accuracy of 6-311G (2d, 2p) basis set, the def2-TZVP was selected for a comparison, as it exhibits an excellent performance for precisely describing molecular properties and reactions.[5] In this study, BDE value of peroxide bond in H_2O_2 was calculated at both SMD/B3LYP-D3/def2-TZVP//B3LYP-D3/6-31G (d, p) and SMD/B3LYP-D3/6-311G (2d, 2p)// B3LYP-D3/6-31G (d, p) level of theory. The result was almost identical (with a slight difference of 0.016 kcal mol^{-1}), indicating the accuracy of 6-311G (2d, 2p) basis set. In addition, 6-311G (2d, 2p) shows much lower computational cost than that of def2-TZVP one.[6] Thus, this basis set was used in this study. Note that BDE values empirically reflect the strength of peroxy bond in gas phase, and may not well represents the chemical processes in aqueous solutions.[7] Therefore, we further analyzed the frontier molecular orbitals of precursors, and calculated other electronic parameters (*i.e.*, bond length, Mayer bond order, and HOMO-LUMO energy gap) for mechanism elucidation of radical formation.

Text S5: Exclusion of interference of SCN^- and phosphate buffer on $\Phi_{\bullet OH}$ determination.

Previous studies proposed that SCN^- can be photolyzed forming $SCN_2^{\bullet-}$, thus SCN^- as a probe may cause interference for $\Phi_{\bullet OH}$ determination monitored at 475 nm.[8] To exclude this interference, a working solution containing only SCN^- at 0.1 M was prepared and irradiated. We measured the full absorption spectrum and the absorption decay at 475 nm after excitation. As illustrated in Figure S4, the transient spectra showed a broad absorption band from 360 to 560 nm, and the absorption peak approximately centers at 460 nm with the maximum absorbance of 0.012. The observation indicated that after excitation SCN^- indeed generates new species. However, the lifetime of the transient species is short at *ca.* 7 μs, which is 3 orders of magnitude shorter than that of $SCN_2^{\bullet-}$, which is on the order of milliseconds.[9] Therefore, the formed species in our system cannot be $SCN_2^{\bullet-}$. However, the identification of this transient species is beyond the scope of this study, and this species will not interfere with our determination of $\Phi_{\bullet OH}$ for radicals due to its the low absorbance (8×10^{-3}) and fast attenuation kinetics.

We also examined the possible influence of phosphate buffer on $\Phi_{\bullet OH}$ by preparing a 10 mM phosphate buffer solution and irradiating it at 266 nm. The full absorption spectrum was also measured from 410 to 520 nm. Based on Figure S5a, there is a slight absorption with complete decay within 3.8 μs. The decay kinetics at 475 nm (the wavelength used for monitoring of $SCN_2^{\bullet-}$) was illustrated in Figure S5b. No discernible absorbance change was observed. Similar to SCN^-, phosphate buffer also does not compromise the precision of $\Phi_{\bullet OH}$ determinations.

Table S1: The bond dissociation enthalpies (BDE, kcal mol^{-1}) of several compounds calculated with different functionals. The dashed line (---) refers to the dissociated bond.

compound	B3LYP-D3	CAM-B3LYP	M06-2X	reported value
CH_3---H	105.9	106.3	106.7	105[10]
H_3C---CH_3	90.61	92.24	95.42	90.0[10]
HO---OH	47.03	47.98	48.78	47.0[11]
$(O_3SO$---$OSO_3)^{2-}$	22.39	25.45	33.69	21.9[12]
$(HO$---$OSO_3)^-$	33.40	37.28	41.99	33.5[13]

Table S2: Comparison of quantum yields (Φ) for different radicals (The determination of Φ in these studies was conducted at room temperature. [a] λ is the excitation wavelength for the precursor; [b] While the literature reports Φ values at different excitation wavelengths, only Φ values specifically centered around 266 nm were tabulated due to the relevance to our study; [c] N.A. refers to not available, as Yang *et al.* measured Φ for $^{\bullet}OH$ and $SO_4^{\bullet-}$ in a O_3/PMS system, and Φ is defined as the yield of radicals per mole of O_3 consumption).

photochemical reaction	radical	λ (nm) [a]	Φ (unitless)	methods	reference
$H_2O_2 + h\nu \rightarrow {}^{\bullet}OH + {}^{\bullet}OH$	$^{\bullet}OH$	266	1.10 ± 0.01	determination of Φ at 475 nm with probe SCN^-	this study
		248	1.0 ± 0.1	derivation from consecutive reactions	Yu *et al.*[8]
		253.7 [b]	1.16 ± 0.05	chemical derivatization required	Goldstein *et al.*[14]
		260 [b]	1.11 ± 0.05	chemical derivatization required	Goldstein *et al.*[14]
PDS + $h\nu \rightarrow SO_4^{\bullet-}$ + $SO_4^{\bullet-}$	$SO_4^{\bullet-}$	266	1.46 ± 0.05	determination of Φ at 450 nm	this study
		248	1.39 ± 0.04	derivations from consecutive reactions	Herrmann *et al.*[15]
		254	1.4 ± 0.1	derivations from pH change	Gertraud *et al.*[16]
		254	1.4	derivations from consecutive reactions	Xie *et al.*[17]
PMS + $h\nu \rightarrow SO_4^{\bullet-}$ + $^{\bullet}OH$	$^{\bullet}OH$	266	0.56	determination of Φ at 450 nm with probe TPA	this study
		N.A. [c]	0.43 ± 0.01	chemical derivatization required	Yang *et al.*[18]
	$SO_4^{\bullet-}$	266	0.57 ± 0.02	determination of Φ at 450 nm	this study
		254	0.52 ± 0.01	derivations from consecutive reactions	Guan *et al.*[19]
		N.A. [c]	0.53 ± 0.01	chemical derivatization required	Yang *et al.*[18]

Table S3: Comparison of peroxy bond characteristics and energies for the selected precursors (BDE for bond dissociation enthalpy in the unit of kcal mol^{-1}; E_{gap} refers to the energy gaps between the HOMO and LUMO of the precursors). The BDE and E_{gap} values were calculated at SMD/B3LYP-D3/6-311G(2d,2p)//B3LYP-D3/6-31G(d,p) level of theory.

precursors	BDE	bond length (Å)	Mayer bond order (unitless)	E_{gap} (eV)
H_2O_2	47.0	1.47	0.95	7.46
PDS	22.4	1.48	0.88	6.73
PMS	33.4	1.47	0.92	7.11

Table S4: Orbital surface plots of •OH (isodensity value = 0.02 e Bohr^{-3}. FO refers to fragment orbital).

orbital index	orbital surface plot
FO 2	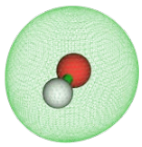
FO 3	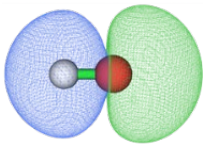
FO 4	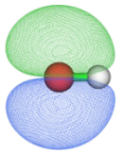
FO 5	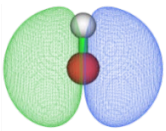
FO 6	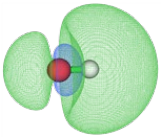

Table S5: Orbital surface plots of $SO_4^{\bullet -}$ (isodensity value = 0.02 e Bohr^{-3}. FO refers to fragment orbital).

orbital index	orbital surface plot
FO 18	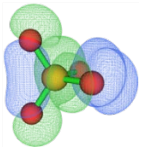
FO 19	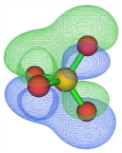
FO 20	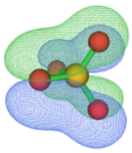
FO 21	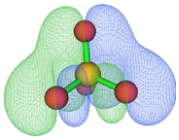
FO 22	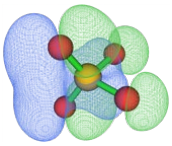
FO 23	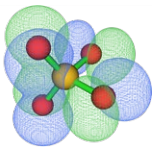
FO 24	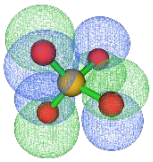
FO 25	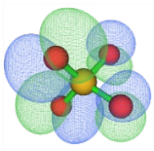

Table S6: Orbital surface plots of H_2O_2 (isodensity value = 0.02 e $Bohr^{-3}$. MO refers to molecular orbital. MO 9 and MO 10 are HOMO and LUMO orbitals, respectively, which are illustrated in Figure 5).

orbital index	orbital surface plot
MO 3	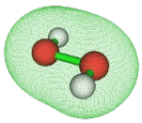
MO 4	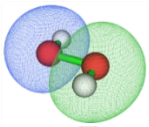
MO 5	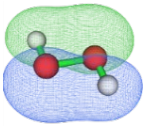
MO 6	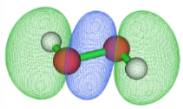
MO 7	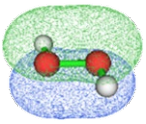
MO 8	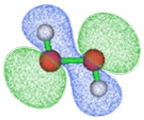
MO 11	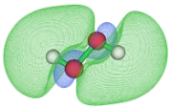
MO 12	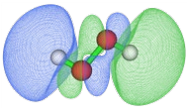

Table S7: Orbital surface plots of PDS (isodensity value = 0.02 e Bohr^{-3}. MO refers to molecular orbital. MO 49 and MO 50 are HOMO and LUMO orbitals, respectively, which are illustrated in Figure 5).

orbital index	orbital surface plot	orbital index	orbital surface plot
MO 37	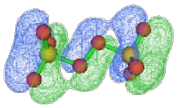	MO 44	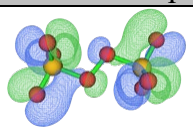
MO 38	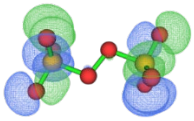	MO 45	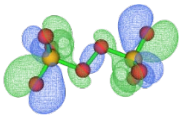
MO 39	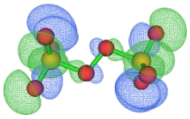	MO 46	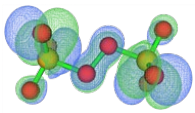
MO 40	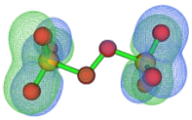	MO 47	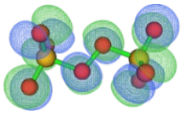
MO 41	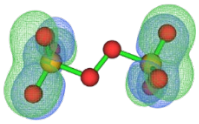	MO 48	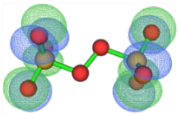
MO 42	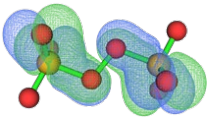	MO 51	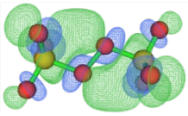
MO 43	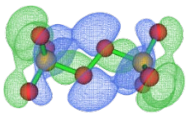	MO 52	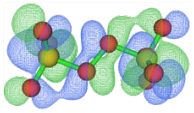

Table S8: Orbital surface plots of PMS (isodensity value = 0.02 e Bohr^{-3}. MO refers to molecular orbital. MO 29 and MO 30 are HOMO and LUMO orbitals, respectively, which are illustrated in Figure 5).

orbital index	orbital surface plot
MO 21	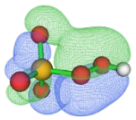
MO 22	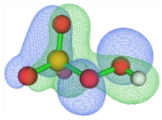
MO 23	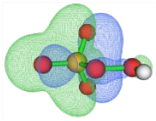
MO 24	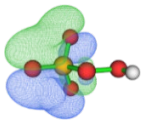
MO 25	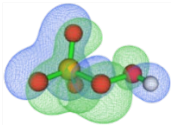
MO 26	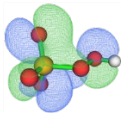
MO 27	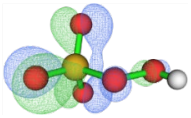
MO 28	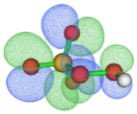

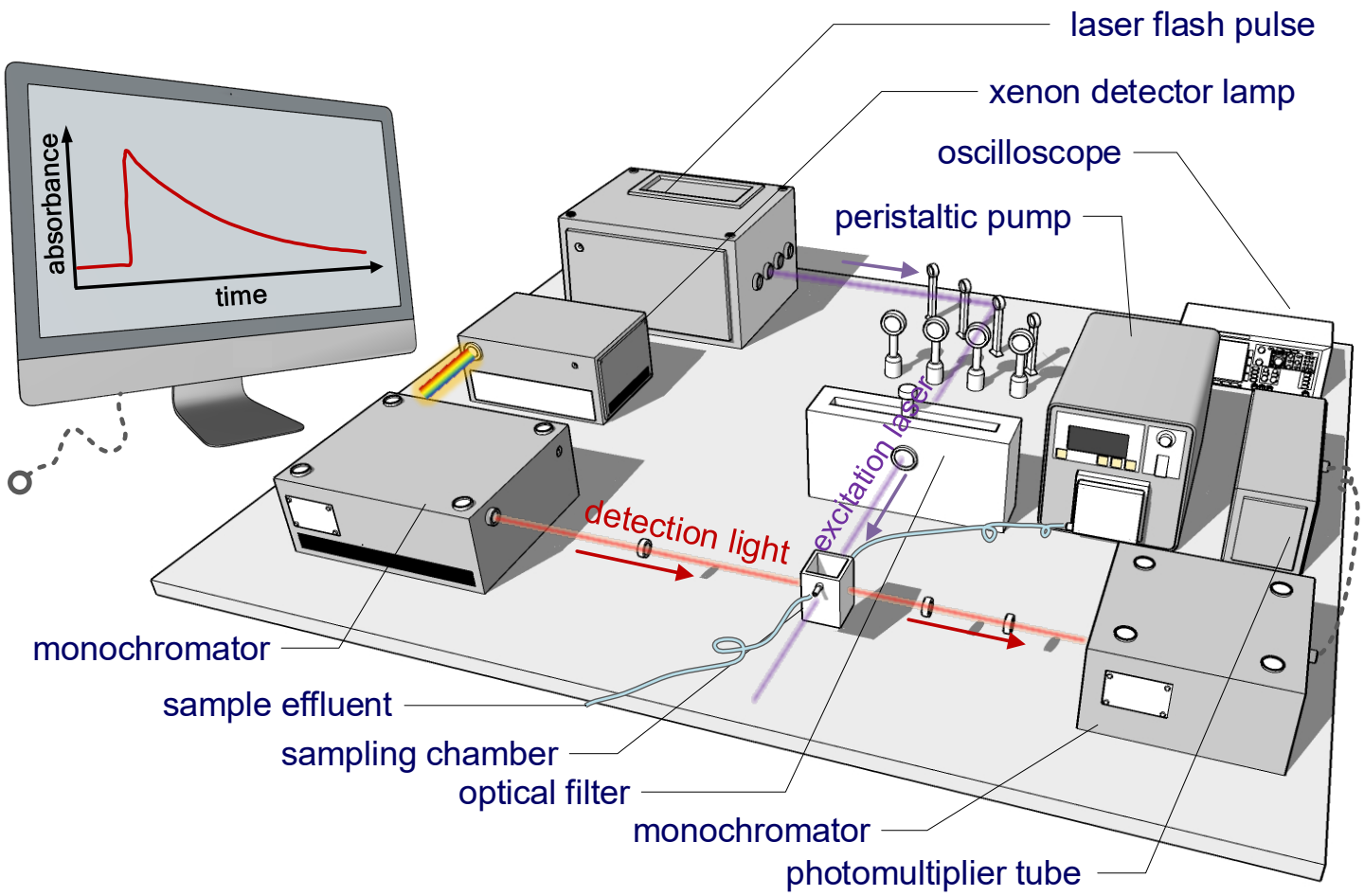

Figure S1: Schematic and workflow diagram of the home-built laser flash photolysis platform.

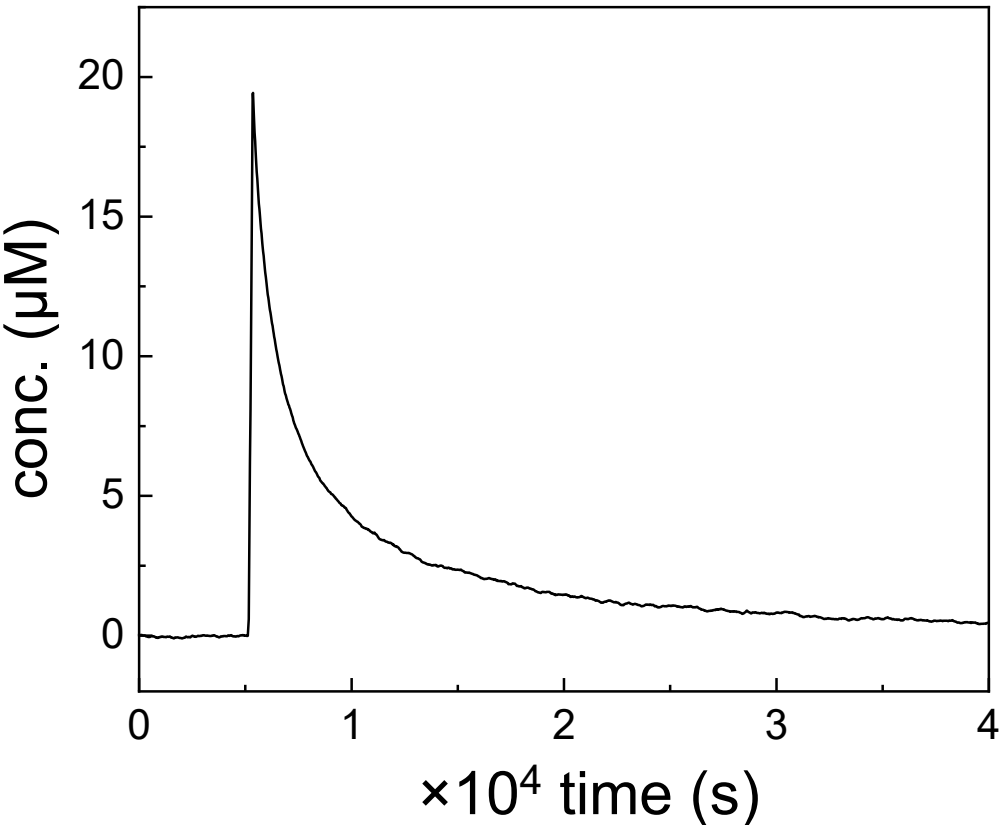

Figure S2: The concentration decay of $SCN_2^{\bullet-}$ monitored at 475 nm based on the evolution of ΔA in Figure 1(b). ($[H_2O_2]$ = 20 mM, $[SCN^-]$ = 5 mM, [phosphate buffer] = 5 mM, pH =7)

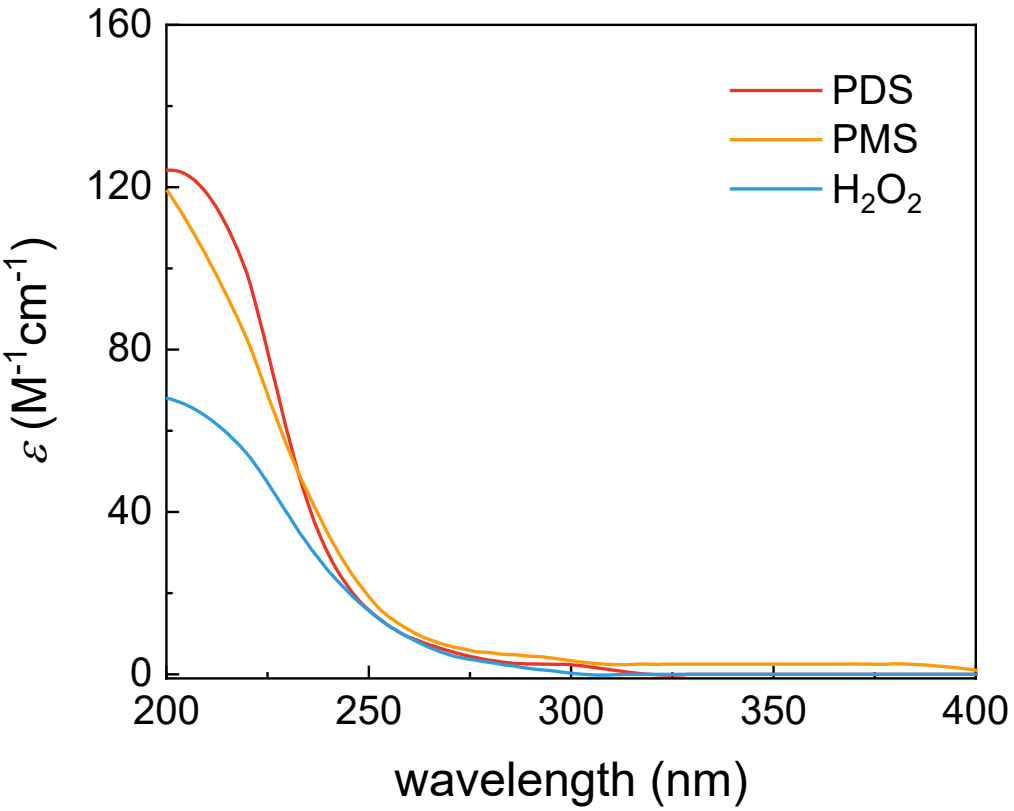

Figure S3: Base-10 molar absorption coefficient (ε) spectra of the three radical precursors at pH 7.

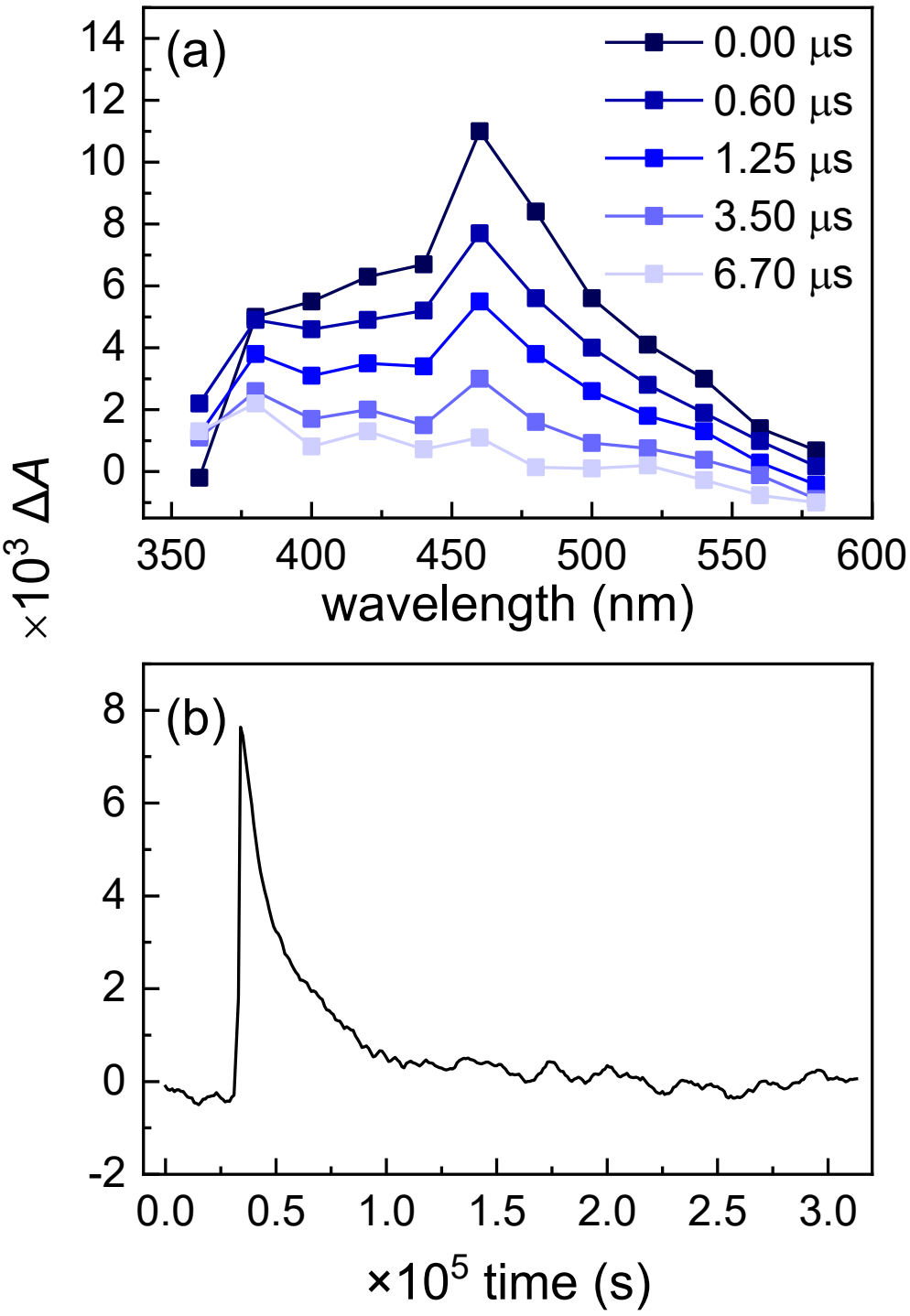

Figure S4: Laser flash photolysis of 0.1 M SCN^- solution. (a) Full absorption spectra were scanned from 360 to 580 nm. (b) Absorption decay monitored at 475 nm.

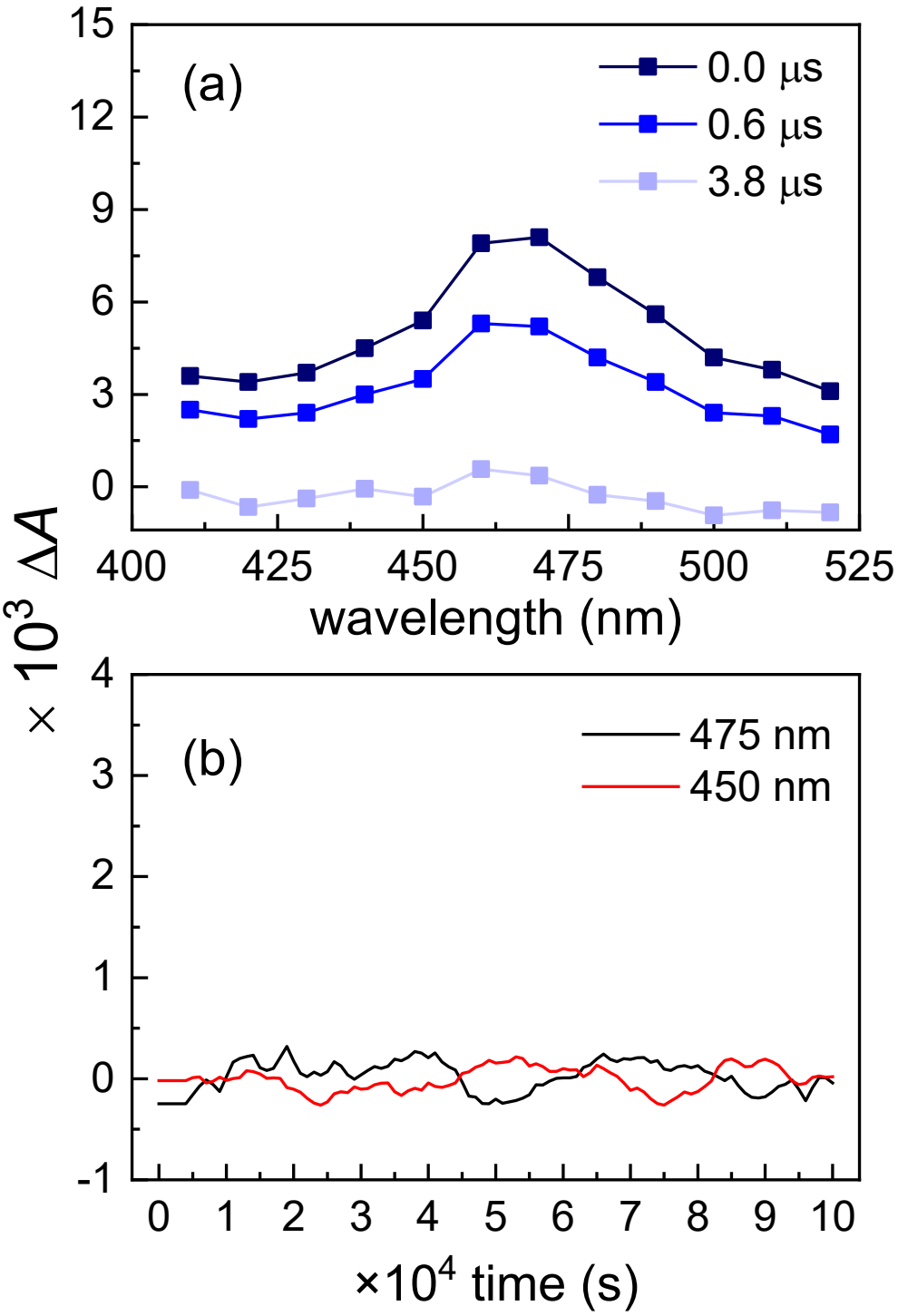

Figure S5: Laser flash photolysis of 10 mM phosphate buffer solution. (a) Full absorption spectra were scanned from 410 to 520 nm. (b) Absorption change monitored at 450 and 475 nm.

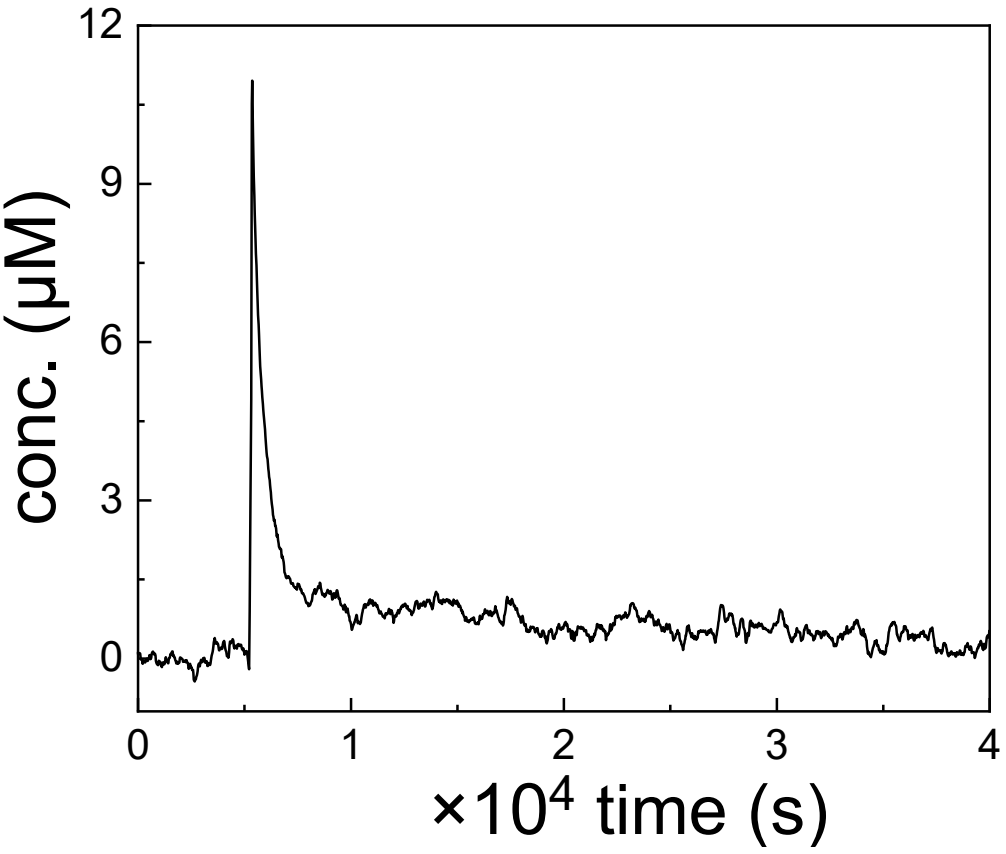

Figure S6: The concentration decay of $SO_4^{\bullet-}$ monitored at 450 nm based on the evolution of ΔA in Figure 1(d). ([PMS] = 20 mM, [phosphate buffer] = 5mM, pH = 7)

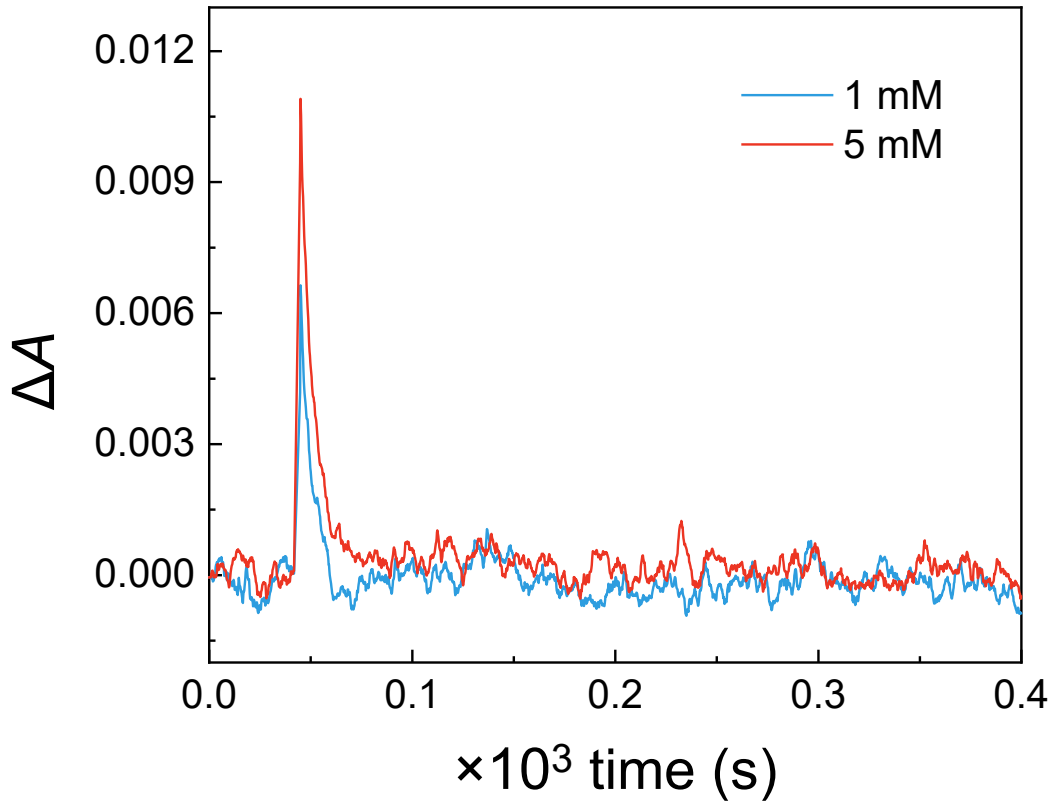

Figure S7: Laser flash photolysis of 20 mM PMS in the presence of 1 and 5 mM of SCN^-. The absorption decay was monitored at 475 nm.

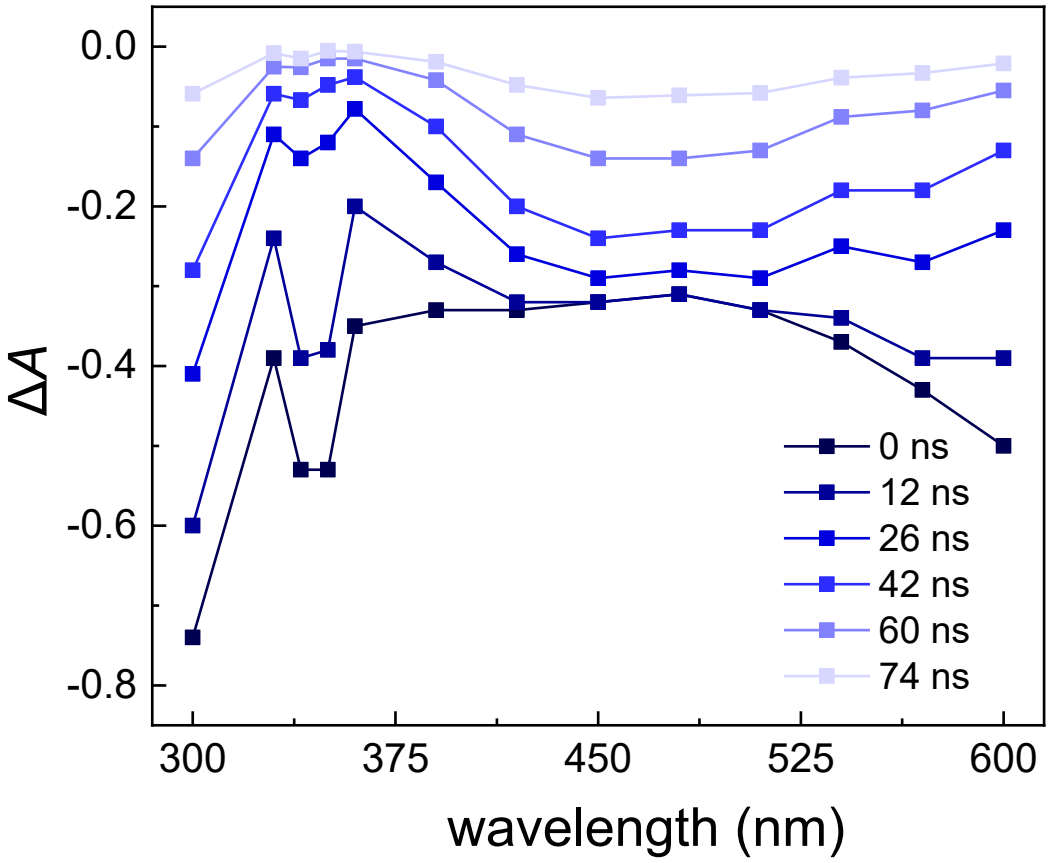

Figure S8: The photolysis of a working solution containing TPA and PMS. ([TPA] = 5 mM, [PMS] = 20 mM, [phosphate buffer] = 5 mM, and pH = 7)

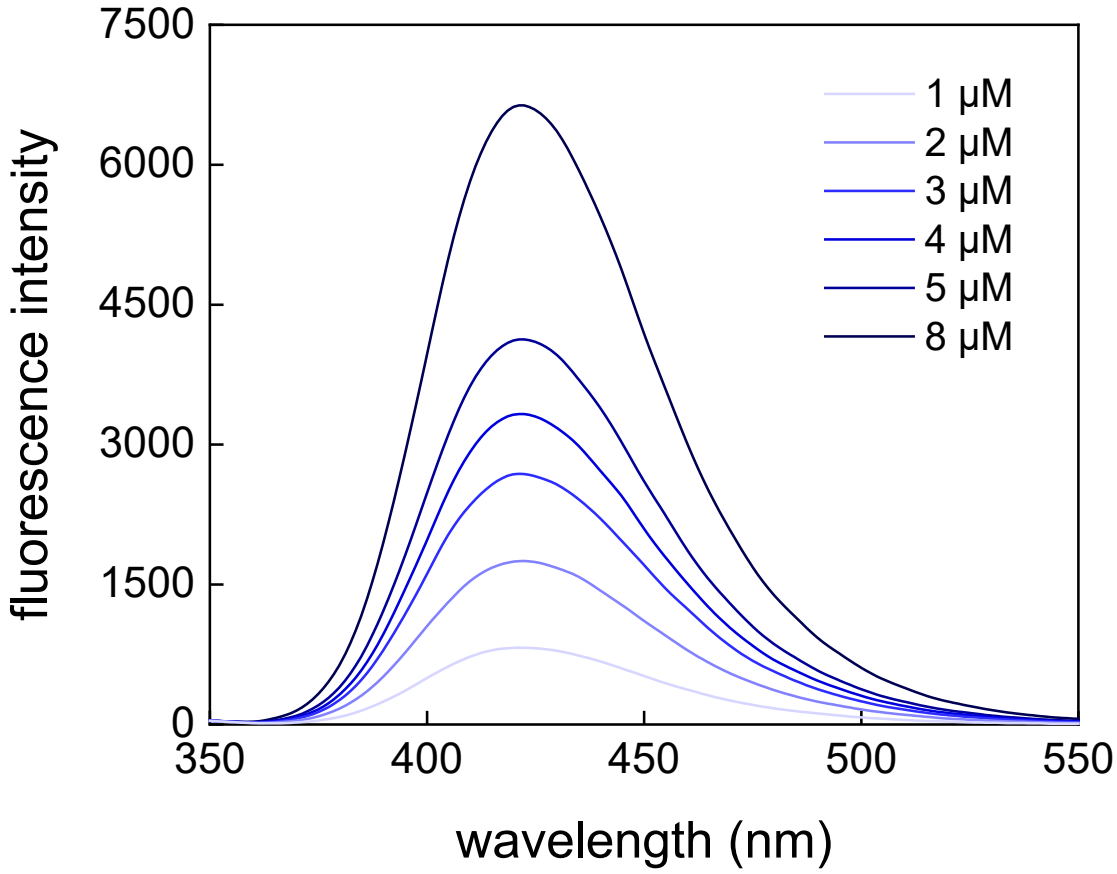

Figure S9: Steady-state fluorescence spectra of hTPA with different concentrations. The emission wavelength was monitored from 350 to 550 nm, and the excitation wavelength was set to be 315 nm.

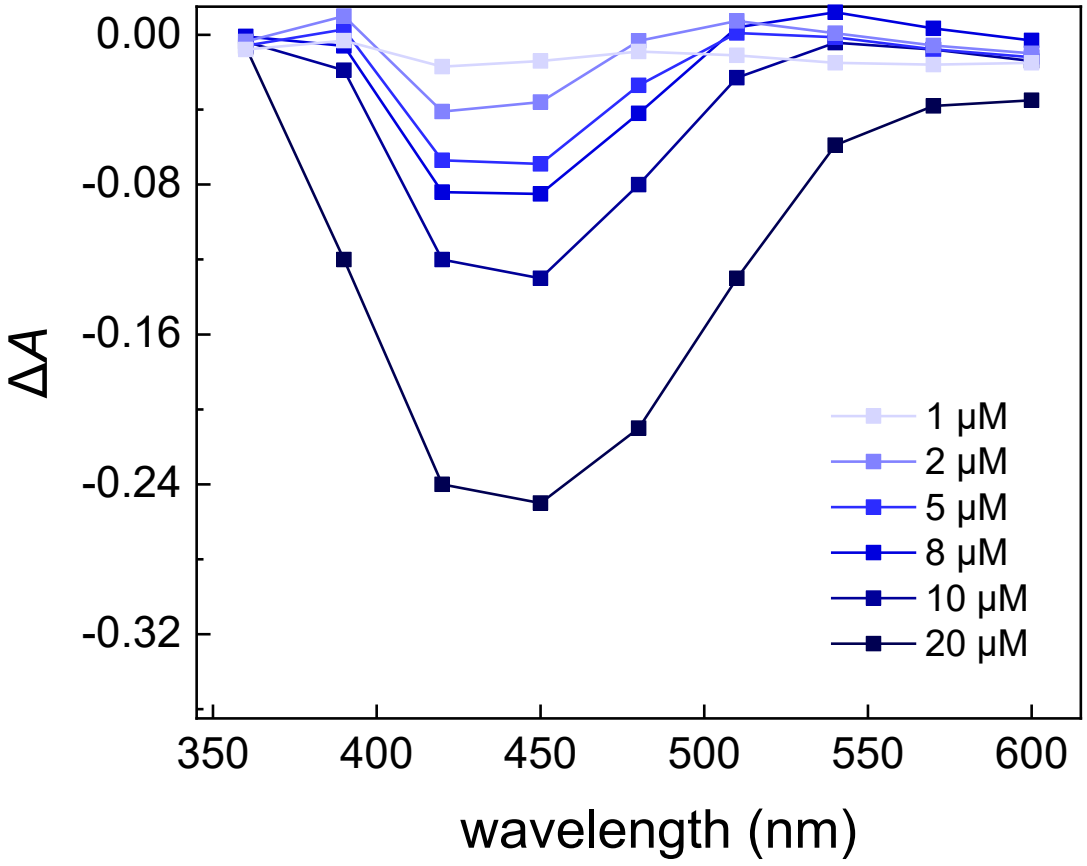

Figure S10: The full absorption spectra of hTPA from 360 nm to 600 nm. ([phosphate buffer] = 5 mM and pH = 7)

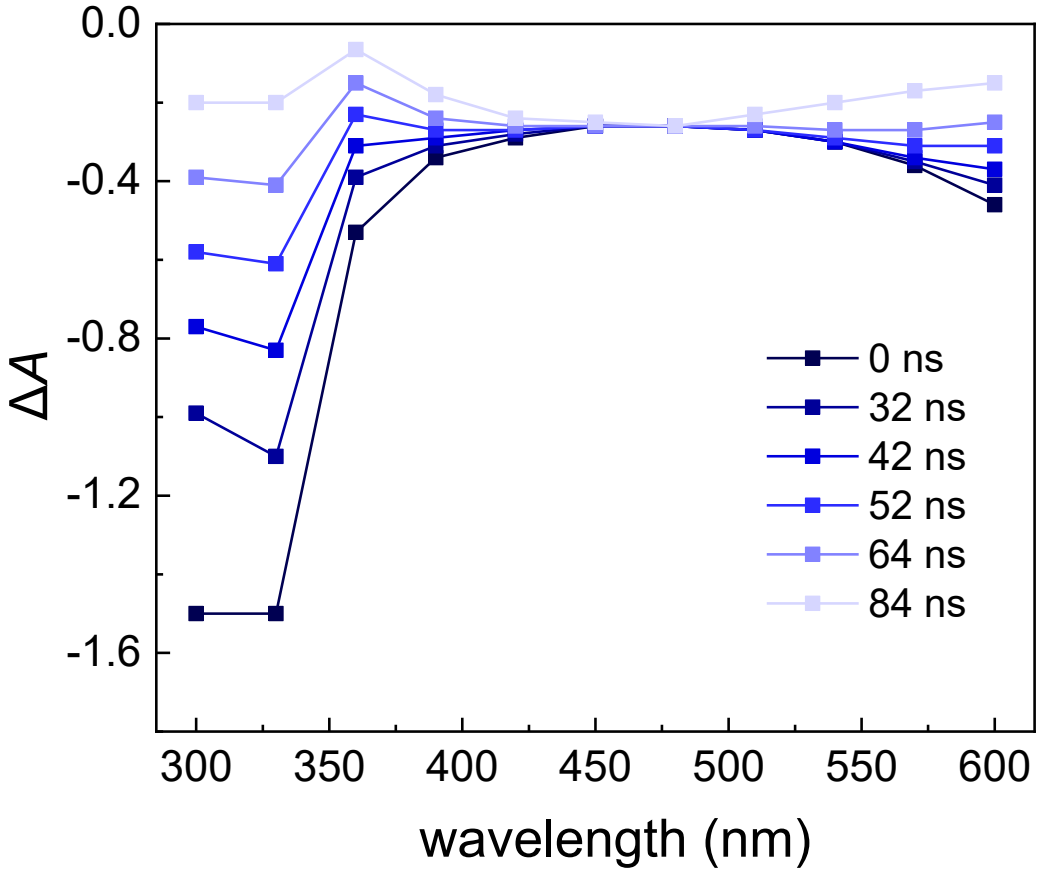

Figure S11: The full absorption spectra of hTPA from 300 to 600 nm. ([phosphate buffer] = 5 mM, [hTPA] = 10 μM, and pH = 7)

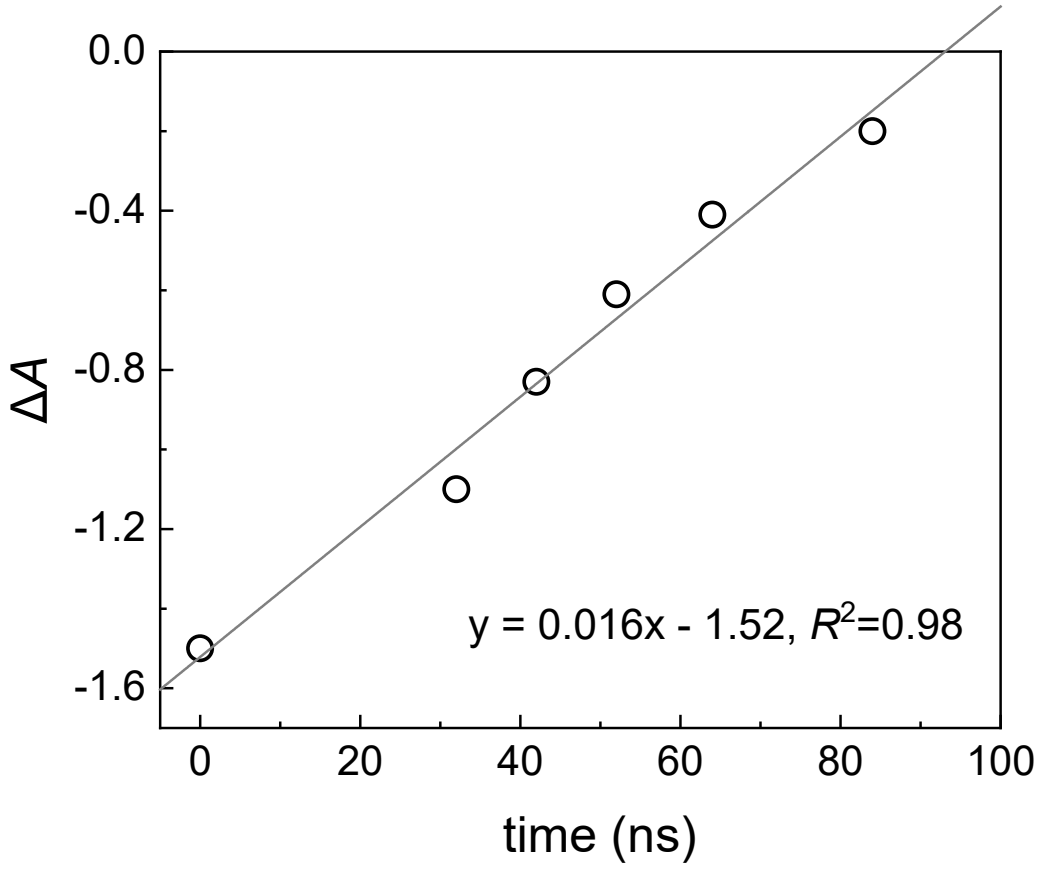

Figure S12: The plot of ΔA values at the wavelength of 330 nm as function of time. ([hTPA]= 10 μM, [phosphate buffer] = 5 mM, and pH = 7)

REFERENCES

1. Klassen, N. V.; Marchington, D.; McGowan, H. C. E., H_2O_2 Determination by the I_3^- Method and by $KMnO_4$ Titration. *Anal. Chem.* **1994,** *66*, (18), 2921-2925.
2. Pędziwiatr, P.; Mikołajczyk, F.; Zawadzki, D.; Mikołajczyk, K.; Bedka, A., Decomposition of hydrogen peroxide - kinetics and review of chosen catalysts. *Acta. Innovations* **2018**, (26), 45-52.
3. Ohlweiler, O. A.; Schneider, A. M. H., Standardization of potassium permanganate by titration of sodium oxalate in presence of perchloric acid and manganese(II) sulfate. *Anal. Chim. Acta* **1972,** *58*, (2), 477-480.
4. Braslavsky, S. E., Glossary of terms used in photochemistry, 3rd edition (IUPAC Recommendations 2006). *Pure Appl. Chem.* **2007,** *79*, (3), 293-465.
5. Xu, X.; Truhlar, D. G., Accuracy of Effective Core Potentials and Basis Sets for Density Functional Calculations, Including Relativistic Effects, As Illustrated by Calculations on Arsenic Compounds. *J. Chem. Theory Comput.* **2011,** *7*, (9), 2766-2779.
6. Bursch, M.; Mewes, J. M.; Hansen, A.; Grimme, S., Best-Practice DFT Protocols for Basic Molecular Computational Chemistry. *Angew. Chem. Int. Ed.* **2022,** *61*, (42), e202205735.
7. Blanksby, S. J.; Ellison, G. B., Bond Dissociation Energies of Organic Molecules. *Accounts of Chemical Research* **2003,** *36*, (4), 255-263.
8. Yu, X.-Y.; Barker, J. R., Hydrogen Peroxide Photolysis in Acidic Aqueous Solutions Containing Chloride Ions. II. Quantum Yield of $HO^{\bullet}$(Aq) Radicals. *J. Phys. Chem. A* **2003,** *107*, (9), 1325-1332.
9. Milosavljevic, B. H.; LaVerne, J. A., Pulse Radiolysis of Aqueous Thiocyanate Solution. *J. Phys. Chem. A* **2005,** *109*, (1), 165-168.
10. Ruscic, B., Active Thermochemical Tables: Sequential Bond Dissociation Enthalpies of Methane, Ethane, and Methanol and the Related Thermochemistry. *J. Phys. Chem. A* **2015,** *119*, (28), 7810-7837.
11. Bach, R. D.; Ayala, P. Y.; Schlegel, H. B., A Reassessment of the Bond Dissociation Energies of Peroxides. An ab Initio Study. *J. Am. Chem. Soc.* **1996,** *118*, (50), 12758-12765.
12. Peng, W.; Dong, Y.; Fu, Y.; Wang, L.; Li, Q.; Liu, Y.; Fan, Q.; Wang, Z., Non-radical reactions in persulfate-based homogeneous degradation processes: A review. *Chem. Eng. J.* **2021,** *421*.
13. Wang, J.; Wang, S., Activation of persulfate (PS) and peroxymonosulfate (PMS) and application for the degradation of emerging contaminants. *Chem. Eng. J.* **2018,** *334*, 1502-1517.
14. Goldstein, S.; Aschengrau, D.; Diamant, Y.; Rabani, J., Photolysis of Aqueous H_2O_2: Quantum Yield and Applications for Polychromatic UV Actinometry in Photoreactors. *Environ. Sci .Technol.* **2007,** *41*, (21), 7486-7490.
15. Herrmann, H., On the photolysis of simple anions and neutral molecules as sources of O^-/OH, SO_x^- and Cl in aqueous solution. *Phys. Chem. Chem. Phys.* **2007,** *9*, (30), 3935-3964.
16. Mark, G.; Schuchmann, M. N.; Schuchmann, H.-P.; von Sonntag, C., The photolysis of potassium peroxodisulphate in aqueous solution in the presence of *tert*-

butanol: a simple actinometer for 254 nm radiation. *J. Photochem. Photobiol. A: Chem.* **1990,** *55*, (2), 157-168.
17. Xie, P.; Ma, J.; Liu, W.; Zou, J.; Yue, S.; Li, X.; Wiesner, M. R.; Fang, J., Removal of 2-MIB and geosmin using UV/persulfate: contributions of hydroxyl and sulfate radicals. *Water Res.* **2015,** *69*, 223-233.
18. Yang, Y.; Jiang, J.; Lu, X.; Ma, J.; Liu, Y., Production of sulfate radical and hydroxyl radical by reaction of ozone with peroxymonosulfate: a novel advanced oxidation process. *Environ. Sci. Technol.* **2015,** *49*, (12), 7330-9.
19. Guan, Y. H.; Ma, J.; Li, X. C.; Fang, J. Y.; Chen, L. W., Influence of pH on the formation of sulfate and hydroxyl radicals in the UV/peroxymonosulfate system. *Environ. Sci. Technol.* **2011,** *45*, (21), 9308-14.